Research Article

Computational Approach on Convective-Magneto Trihybrid Nanoflow with Space Dependent Energy Source/Sink: Drug Delivery

B Vinothkumar [ID], T Poornima[*]

Department of Mathematics, School of Advanced Sciences, Vellore Institute of Technology, Vellore-632014, Tamil Nadu, India
E-mail: poornima.t@vit.ac.in

Abstract: Iron oxide, Silver, Aluminium oxide, these nanoparticles individually or combined help in drug delivery especially aluminium oxide nanofluid used in an anti-blood pressure drug called 'Telmisartan'. Alumina and silver particles are used in manufacturing nanocomposites which have more antimicrobial properties. This is the reason for the current study of ternary nanofluids natural convective flow and efficacy of energy transfer in a bi-directionally sheet. Currently, ternary nanofluids (Fe_3O_4, Ag, Al_2O_3) are being taken for analysis. Usual water (H_2O) is the conventional base fluid. Two different combinations of ternary nanofluids are used to get the average heat transfer rate, mixture ratios ($Fe_3O_4 + Ag$) and ($Fe_3O_4 + Ag + Al_2O_3$) when subjected to a variety of physical influences, including thermal radiation, magnetic fields, heat production and absorption, and nanoparticle volume amount. It is possible to solve the developed set of equations numerical results using the Keller box (finite differences) method with the help of MATLAB programming. This method helps in solving higher order partial differential equation (PDEs) to ordinary differential equation (ODEs). The investigations findings demonstrated that the ternary hybrid nanofluids specific heat capacity is directly impacted by temperature. Numerical solutions for Nusselt number, velocity profile, skin friction coefficient, temperature profiles have represented with the help of graphs and tables. The ternary hybrid nanoflow ($Fe_3O_4 + Ag + Al_2O_3/H_2O$) transmits more energy for increasing volume fractions, comparing to the hybrid nanofluid ($Fe_3O_4 + Ag/H_2O$). The study reveals the fact that metal oxides transfer more heat from the system than that of metals. The estimated error of heat transfer rate is higher in alumina nanoflow followed by silver and iron oxide nanofluid flows. The streamlines are equally spaced, but the energy flow amount is higher for the case $M, S = 1$ than $M, S = 2$. But in the case of stretching ratio parameter, the amount energy flow in $\alpha = 0.5 > \alpha = 1.0$. An equal amount of energy flow is observed for varied Biot number.

Keywords: ternary nanofluid, Keller-Box numerical method, stretching sheet, asymmetric energy generation/absorption, magnetic field, radiation

MSC: 35Q79

Nomenclature

Dimensional Variables		Non-Dimensional Variables	
u, v, w, x & y	Velocity components & axes	η	Similarity variable
β	Casson parameter	f, g	Stream function
B_0	Magnetic field strength	θ	Temperature
T	Local Temperature	M	Magnetic force
T_w, T_∞	Wall and Ambient Energy	Rd	Radiation
ρ	Density (kg/m^3)	Pr	Prandtl number
μ, v	Dynamic & Kinematic viscosity	Bi	Thermal conjugate parameter
α	Thermal diffusivity	α	Stretching ratio
h_t	Wall heat transfer coefficient	S	Unsteadiness parameter
K	Thermal conductance (W/m K)	Nu	Wall heat transfer rate
$v_w u_w$	Stretching Velocities	C_f	Wall friction
$k*$	Coefficient of mean absorption	Re	Reynolds number
$\sigma*$	Stefan-Boltzmann constant	A_1, A_2, A_3, A_4	Constants
τ_w	Shear stress	ϕ_1, ϕ_2, ϕ_3	Fe$_2$O$_3$, Al$_2$O$_3$, Ag nanoparticle volume fraction
θ_w	Energy flux		s1, s2, s3 Solid nanoparticles
q_r	Radiative heat flux	Suffix	thnf, nf, f Ternary, nano, fluids
$n, a, b, c, a_0, b_0, A, B, h_0$	Constants	r, s	Thermal indices
		HNF	Hybrid nanofluids
σ	Electrical conductivity(s/m)	THNF	Ternary Hybrid Nanoflows
		KBM	Keller Box Method
		RKM	Runge-Kutta Method
	Abbreviations	BL	Boundary Layer
C_p	Energy capacitance (J/kg K)	ODE	Ordinary Differential Equation
		PDE	Partial Differential Equations

1. Introduction

To address the requirements and expectations of the work, researchers have focused their efforts on creating new energy measurements across time. Their goal is to design systems with the greatest heat transfer possible. Applications in the extrusion of polymer sheets from a dye and the drawing of plastic films highlight the significance of viscous fluid flow across a stretched sheet. In order to achieve the necessary thickness, molten silt is issued and then stretched throughout the manufacturing process of these sheets. To achieve the intended product properties, the stretching procedure and cooling rate have a significant influence. Sakiadis et al. [1] first looked at behaviour of boundary layers on continuous solid surfaces. Li et al. [2] discussed on analysis of the ternary nanofluid flow across a stretched sheet. Souayeh et al. [3] examined ternary nanoflow over an exponential extensible sheet. Devi et al. [4] analysed the extending sheet exposed to Newtonian heating affected by Lorentz force. Prasad et al. [5] investigated the variable fluid characteristics effects on heat transmission and MHD flow over a stretched sheet with varying thickness.

The nanofluids that Choi introduced and developed were used as heat transfer fluids in a variety of sectors to speed up the evacuation of heat from a system [6]. Using nanoparticles to improve fluids thermal conductivity. Khan et al. [7] completed the first research on the Nanofluid boundary-layer flow past a stretched sheet. Alrihieli et al. [8] analysed the dissipative properties are affected by concentration, slip, and heat. Stretching sheet-induced Casson-Maxwell nanofluid flow. Kumar et al. [9] investigated the water/Ag-Al_2O_3 hydromagnetic hybrid nanofluid irreversibility investigation across a stretched sheet. Rao et al. [10] analysed the analytical investigation of heat transfer for radiation-heated Casson nanoflow over a porous stretched sheet. Elatter et al. [11] examined the discharge concentration of waste in Eyring-Powell nanoflow through a deformable horizontal plane surface. Sumathi et al. [12] analysed the impact of radiation on Casson Nanofluid flow across an inclined slanted surface. Sharanayya et al. [13] investigated Casson Nanoflow over a stretching sheet with Soret and Heat source/sink imbedded in permeable media. Najiyah et al. [14] analysed a non-linearly permeable shrinking sheet in three dimensions with bidirectional nanofluid flow and MHD radiation.

The mechanical properties of the finished product are impacted when a sheet is stretched because the elastic material taken on a unidirectional orientation. Foresaid study has only addressed 2D boundary layer issues resulting from unidirectional stretching. A standard base fluid combined with more than one type of nanoparticle is referred to as a mixed nanofluid. Due to their unique features, hybrid nanofluids have been proven to perform better in terms of heat transmission than traditional fluids. Hybrid nanofluids are also dependable and reasonably priced. Hayat et al. [15] analysed the Fe_3O_4 and Al_2O_3 immersed thin film flow on stretching surface. Isa et al. [17] investigated the alumina and copper nanoparticle-suspended water-based hybrid nanoflow. Reddy et al. [18] analysed the mass-energy transport properties of a hybrid nanofluid across a stretching or shrinking sheet with slip effects. Alabdulhadi et al. [19] analysed the asymmetrical thin film flow of Al_2O_3/Water nanofluid across an inclined stretching sheet. Javad zadeh et al. [20] described the immunisation of Al_2O_3 and Fe_3O_4 nanoparticles on chitosan and cellulose nanopapers for the specific adsorption of free fatty acids from refined oil.

Heat loses or heat gain in a fluid flow process occurs frequently. It is an inevitable factor when we study energy and species transfer system in a boundary layer theory. Quite good examples of these situations are in building designs, in computers, the CPU, electronic circuits, etc. This generation concept is to enhance the fluid conductivity whilst the other reduces fluid energy. Its term is inevitable only when there finds a huge temperature difference and because of this property, energy generation/absorption has greater importance in MHD flows. Fewer applications are in functioning of brain i.e., in neurobiology, magnetized employment of energy generation/absorption has a crucial role. These applications were well discussed by the researchers in their early works [21-23]. Paul et al. [24] thermally stratified Cu-Al_2O_3/water hybrid nanofluid flows over a vertically extending cylinder under the influence of an angled magnetic field and a heat source or sink. Asogwa et al. [25] studied the magnetic and radiation nanofluids past a Riga plate with a heat sink that accelerates exponentially. Alqawasmi et al. [26] discoursed an analytical method for ternary hybrid nanofluid flow across a disc using a nonlinear heat source-sink and Fourier heat flux model. Singh et al. [35] analysed Ternary hybrid nanofluid (TiO_2-SiO_2-MoS_2/kerosene oil) flow over a rotating disk with quadratic thermal radiation and Cattaneo-Christov model. Yaseen Moh et al. [36] analysed Ternary hybrid nanofluid flow containing gyrotactic microorganisms over three different geometries with Cattaneo-Christov model. Rawat et al. [37] discoursed the Designing soft computing algorithms to study heat transfer simulation of ternary hybrid nanofluid flow between parallel plates in a parabolic trough solar collector: case of artificial neural network and particle swarm optimization. Ali et al. [38]

analysed the Significance of Brownian motion and thermophoresis influence on dynamics of Reiner-Rivlin fluid over a disk with non-Fourier heat flux theory and gyrotactic microorganisms. Khan et al. [39] studied the Magnetic dipole and thermal radiation impacts on stagnation point flow of micropolar based nanofluids over a vertically stretching sheet.

The foremost purpose of the present exploration is to provide a scientific contribution in literature by considering the consequence of convective heat transport in bidirectional water driven hybrid-class Ternary nanofluid using nanoparticles (Fe_3O_4 + Ag + Al_2O_3/H_2O) under the magnetohydrodynamics process. has a lot of applications in semiconducting materials science, (Ag) has also a variety of applications in this modern world. The key applications are as follows for (Al_2O_3) Plastics, rubber, ceramics, refractory products, to improve ceramics density, smoothness, fracture toughness, creep resistance, thermal fatigue resistance, and polymer products wear resistance, Ideal material of far-infrared emission. Packaging materials, cutting tools, high purity crucible, winding axle, and furnace tubes, polishing materials, glass products, metal products, semiconductor materials, Plastic, tape, and grinding belts. Silver nanoparticles (Ag) are increasingly used in various fields, including medical, food, health care, consumer, and industrial purposes, due to their unique physical and chemical properties. These include optical, electrical, and thermal, high electrical conductivity, and biological properties. The application of Fe_3O_4 nanotechnology in many medical areas has been widely developed, especially in the field of drug/gene delivery.

The use of nanoparticles as carrier systems for drugs or other bioactive therapeutic molecules has been investigated with the aim of improving the therapeutic effect and administration of the loaded agents and reducing their side effects. Among these nanoparticles, Fe_3O_4 nanoparticles (NPs) are used extensively in various fields, including biotechnology, biosensing, catalysis, magnetic fluids, separation techniques, energy storage, and environmental modification. Applications of Fe_3O_4 NPs in the field of biotechnology involve targeted drug/gene delivery [27], magnetic resonance imaging (MRI) [28]. Targeted drug/gene delivery systems are particularly beneficial due to their unique magnetic properties, extremely low toxicity, excellent biocompatibility, good biodegradability, and reactive surface that can be readily modified with biocompatible coatings.

From the above survey, it is clear that no work on comparing different combinations of nanoparticles and their thermal conductivity efficacy under natural convection. So, the present work carries out convective-magneto hybrid radiative nanoflow past a bidirectional stretching surface. The modelled boundary layer equations are untangled with Thomas Algorithm. The graphs and tables portray the numerically computed values of different physical parameters on flow field affecting and interested engineering quantities.

2. Mathematical formulation

Consider an unsteady bidirectional magnetohydrodynamics (MHD) flow of hybrid-class ternary nanofluid (Fe_3O_4, Ag, Al_2O_3) touching a stretching obstacle with the incorporation of convective heat transport in xy-plane. It is supposed that the device is stretched in both x- and y-directions with velocities $u_w = \dfrac{ax}{1-ct}$; $a > 0$, $c \geq 0$ and $v_w = \dfrac{by}{1-ct}$; $b \geq 0$, respectively. However, the region covered by the hybrid-class (Fe_3O_4, Ag, Al_2O_3) ternary nanofluid is above the xy-plane. Velocity components in x, y and z directions are signified by u, v and w, respectively. Figure 1 describes the graphical abstract of the present investigation.

A Newtonian hybrid nanoflow along a bidirectional extensible surface with the following assumptions is taken for study:

1. Unsteady, three-dimensional incompressible flow.

2. Surface is extended along x-axis with a stretching velocity $u_w = \dfrac{ax}{1-ct}$; $a > 0$, $c \geq 0$ and along the y-axis, the flow passes at a speed of $v_w = \dfrac{by}{1-ct}$; $b \geq 0$, normal to the flow.

3. The temperature of the fluid near the surface is $T_w = T_\infty + a_0 \left(\dfrac{x^r y^s}{1-ct} \right)$.

4. An uneven magnetic force of strength $B_0(t) = \dfrac{b_0}{\sqrt{1-ct}}$ applied normal i.e., along z-axis.

5. The fluid medium is filled with ferrous, aluminium oxides and silver NPs with water as base fluid.

6. The system is exposed to radiation and an asymmetric energy generation/absorption is considered.

7. Wall surface is allowed for convection with a coefficient $h_t = h_0/(1-ct)$.

8. Induced magnetic field is neglected and because of the flat plate buoyant forces are feeble, so avoided.

The Schematic representation of this physical model is shown in the Figure 1.
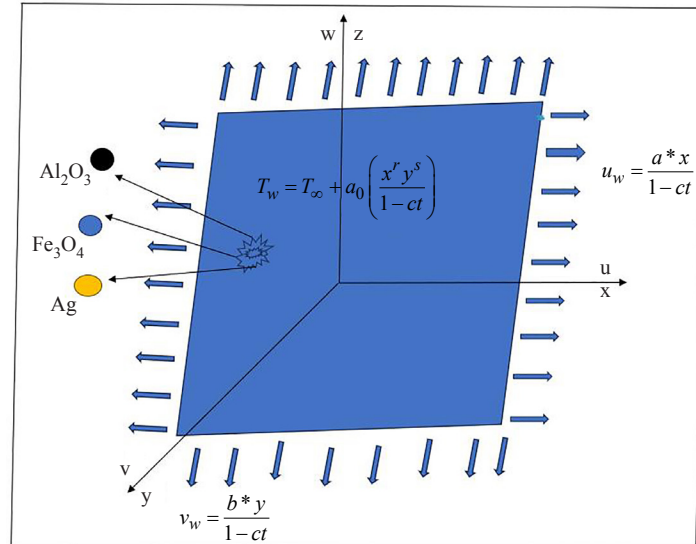

Figure 1. The problem's physical configuration

The above assumptions lead to the system of equations which obeys the present situation and follows the literature [29-31].

Governing equations:

$$\frac{\partial u}{\partial t} + \frac{\partial v}{\partial y} + \frac{\partial w}{\partial z} = 0, \tag{1}$$

$$\frac{\partial u}{\partial t} + u\frac{\partial u}{\partial x} + v\frac{\partial u}{\partial y} + w\frac{\partial u}{\partial z} = \frac{\mu_{thnf}}{\rho_{thnf}}\frac{\partial^2 u}{\partial z^2} - \frac{\sigma_{thnf}}{\rho_{thnf}}B_0^2 u, \tag{2}$$

$$\frac{\partial v}{\partial t} + u\frac{\partial v}{\partial x} + v\frac{\partial v}{\partial y} + w\frac{\partial v}{\partial z} = \frac{\mu_{thnf}}{\rho_{thnf}}\frac{\partial^2 v}{\partial z^2} - \frac{\sigma_{thnf}}{\rho_{thnf}}B_0^2 v, \tag{3}$$

$$\frac{\partial T}{\partial t} + u\frac{\partial T}{\partial x} + v\frac{\partial T}{\partial y} + w\frac{\partial T}{\partial z} = \alpha_{thnf}\frac{\partial^2 T}{\partial z^2} - \frac{\mu_{thnf}}{\left(\rho c_p\right)_{thnf}}\frac{\partial q_r}{\partial z} + \frac{q'''}{\left(\rho c_p\right)_{thnf}}. \tag{4}$$

Where:

$$q''' = \frac{ku_w}{vx}\left(\left(f'(T_w - T_\infty)A\right) + \left(B(T - T_\infty)\right)\right). \tag{5}$$

The problem's boundary conditions are given as follows:

$$u = \frac{a^*x}{1-ct} = u_w,\; v = V_w = \frac{b^*y}{1-ct},\; w=0,\; -k_f\left(\frac{\partial T}{\partial z}\right) = h_t(T_w - T) \text{ at } z=0,$$

$$u \to 0,\; v \to 0,\; T \to T_\infty \text{ as } z \to \infty. \tag{6}$$

Using the self-similarity analysis [31]

$$\eta = \sqrt{\frac{a^*}{v_f(1-ct)}}\,z,\; u = \frac{a^*x}{(1-ct)}f'(\eta),\; v = \frac{a^*y}{(1-ct)}g'(\eta),$$

$$w = -\sqrt{\frac{a^*v_f}{(1-ct)}}\left(f(\eta) + g(\eta)\right),\; T = T_\infty + (T_w - T_\infty)\theta(\eta). \tag{7}$$

Optically thick fluids need the Rosseland heat approximation for T^4 linearized using Taylor's series about T_∞ i.e., $T^4 = 4TT_\infty^3 - 3T_\infty^4$ is given below:

$$q_r = -\frac{4\sigma^*}{3k^*}\frac{\partial\left(4TT_\infty^3 - 3T_\infty^4\right)}{\partial z}. \tag{8}$$

Substituting Eqn. (8) in Eq. (4) gives rise to the following form

$$\frac{\partial T}{\partial t} + u\frac{\partial T}{\partial x} + v\frac{\partial T}{\partial y} + w\frac{\partial T}{\partial z} = \frac{ku_w}{vz}\left(f'(T_w - T_\infty)A + B(T - T_\infty)\right) + \left(\alpha_{Thnf} + \frac{16\sigma^*T_\infty^3}{3k^*\rho c_p}\right)\frac{\partial^2 T}{\partial z^2}. \tag{9}$$

Using the similarity variables (Eq. (7)), the following expression may be used to represent Eqns. (2), (3), (9):

$$A_1 f''' - (f')^2 + (f+g)f'' - S\left(f' + \frac{\eta}{2}f''\right) - A_2 M f' = 0, \tag{10}$$

$$A_1 g''' - (g')^2 + (f+g)g'' - S\left(g' + \frac{\eta}{2}g''\right) - A_2 M g' = 0, \tag{11}$$

$$A_3\,\theta''\left(1 + \frac{4}{3}F\right) + \Pr\left((f+g)\theta' - (r f' + s g')\theta - S\left(\theta + \frac{\eta}{2}\theta'\right) + A_3(Af' + B\theta)\right) = 0. \tag{12}$$

According to the relevant boundary conditions (Eq. (6))

$$f(\eta) + g(\eta) = 0, f'(\eta)=1, g'(\eta)=\alpha, \theta'(\eta)=-Bi(1-\theta) \text{ at } \eta = 0,$$

$$f'(\eta)\to 0, g'(\eta)\to 0, \theta(\eta)\to 0 \text{ as } \eta\to\infty. \tag{13}$$

The following is a description of the characterising parameters.

$$M = \frac{\sigma_f b_0^2}{\rho_f a^*}, Bi = \frac{h_0}{k_f}\sqrt{\frac{v_f}{a^*}}, S = \frac{c}{a^*}, \alpha = \frac{b^*}{a}, \text{ Pr} = \frac{(c_p)_f \mu_f}{k_f},$$

$$A_1 = \frac{\mu_{thnf}}{\rho_f}, A_2 = \frac{\sigma_{thnf}}{\sigma_f}, A_3 = \frac{k_{thnf}}{k_f}, F = \frac{4\sigma^* T_\infty^3}{k^* k}. \tag{14}$$

The following may be used to express the local Nusselt numbers and skin friction coefficient along axial and longitudinal directions Ahmad et al. [30].

$$C_{fx} = \frac{\tau_{wx}}{\rho_{hnf}}, C_{fy} = \frac{\tau_{wy}}{\rho_{hnf} V_w^2},$$

$$Nu_x = \left(1+\frac{4}{3F}\right)\frac{x q_w}{k_f(T_w-T_\infty)} \text{ and } Nu_y = \left(1+\frac{4}{3F}\right)\frac{y q_w}{k_f(T_w-T_\infty)}. \tag{15}$$

Where:

$$\tau_{wx} = \mu_{thnf}\left(\frac{\partial u}{\partial z}\right)_{z=0}, \tau_{wy} = \mu_{thnf}\left(\frac{\partial v}{\partial z}\right)_{z=0}, q_w = -k_{thnf}\left(\frac{\partial T}{\partial z}\right)_{z=0}. \tag{16}$$

Equations (7) and (16) help Equation (15) to bring in the following expressions Ahmad et al. [30].

$$\sqrt{Re_x}C_{fx} = A_1 f''(0); \sqrt{Re_y}C_{fy} = \alpha^{-3/2} A_1 g''(0),$$

$$(Re_x)^{-1/2} Nu_x = -\left(1+\frac{4}{3F}\right)\frac{k_{thnf}}{k_f}\theta'(0),$$

$$(Re_y)^{-1/2} Nu_y = -\left(1+\frac{4}{3F}\right)\alpha^{-\frac{1}{2}}\frac{k_{thnf}}{k_f}\theta'(0). \tag{17}$$

The following formula yields the heat transfer rate Estimated error (ER) [30].

$$E_R = \frac{\mathrm{Re}_x^{-1/2} Nu\left(Nanofluid\right) - \mathrm{Re}_x^{-1/2} Nu\left(Base\ fluid\right)}{\mathrm{Re}_x^{-1/2} Nu\left(Base\ fluid\right)} \times 100 \tag{18}$$

The thermophysical characteristics of (TiO$_2$, SiO$_2$, Al$_2$O$_3$/H$_2$O) Tri hybrid nanofluid are Manjunatha et al. [32].

Density	$\rho_{thnf} = \left(1-\phi_1\right)\left\{\left(1-\phi_2\right)\left[\left(1-\phi_3\right)\rho_f + \phi_3\rho_3\right] + \phi_2\rho_2\right\} + \phi_1\rho_1$
Viscosity	$\mu_{thnf} = \dfrac{\mu_f}{\left(1-\phi_1\right)^{2.5}\left(1-\phi_2\right)^{2.5}\left(1-\phi_3\right)^{2.5}}$
Thermal conductivity	$\dfrac{k_{thnf}}{k_{hnf}} = \dfrac{k_1 + 2k_{hnf} - 2\phi_1\left(k_{hnf} - k_1\right)}{k_1 + 2k_{hnf} + \phi_1\left(k_{hnf} - k_1\right)}$ Where: $\dfrac{k_{hnf}}{k_{nf}} = \dfrac{k_2 + 2k_{nf} - 2\phi_2\left(k_{nf} - k_2\right)}{k_2 + 2k_{nf} + \phi_2\left(k_{nf} - k_2\right)}$ $\dfrac{k_{nf}}{k_f} = \dfrac{k_3 + 2k_f - 2\phi_3\left(k_f - k_3\right)}{k_3 + 2k_f + \phi_3\left(k_f - k_3\right)}$
Electrical conductivity	$\dfrac{\sigma_{thnf}}{\sigma_{hnf}} = \dfrac{\left(1+2\phi_1\right)\sigma_1 + \left(1-2\phi_1\right)\sigma_{hnf}}{\left(1-\phi_1\right)\sigma_1 + \left(1+\phi_1\right)\sigma_{hnf}}$ Where: $\dfrac{\sigma_{hnf}}{\sigma_{nf}} = \dfrac{\left(1+2\phi_2\right)\sigma_2 + \left(1-2\phi_2\right)\sigma_{nf}}{\left(1-\phi_2\right)\sigma_2 + \left(1+\phi_2\right)\sigma_{nf}}$ $\dfrac{\sigma_{nf}}{\sigma_f} = \dfrac{\left(1+2\phi_3\right)\sigma_3 + \left(1-2\phi_3\right)\sigma_f}{\left(1-\phi_3\right)\sigma_3 + \left(1+\phi_3\right)\sigma_f}$

Table 1. Thermophysical properties of the nanoparticles and the base fluid [33]

	$[kgm^{-1}]\rho$	$[Sm^{-1}]\sigma$	$[W(mk)^{-1}]k$
H_2O	997.1	5.5×10^{-6}	0.6071
Fe_3O_4	5,180	2.5×10^4	9.7
Ag	10,500	6.3×10^7	429
Al_2O_3	6,310	5.965×10^7	35.0

3. Methodology

Following the mathematical modelling of the actual method, the next step is to build the answer to the modelled equation. We opted for Keller-Box approach (KBM), a hidden finite differences methodology, for the computational solution of the modelled equations since it combines second-degree validity with the ability of step size adaptation. Since its quicker convergence rate relative to conventional numerical techniques, this approach is best suited for solving boundary layer flow problems. Using this approach, higher-order PDEs are reduced to first-order PDEs, which are then translated into central difference formulas. The decomposition of LU technique is used to solve the matrix-vector form of transformed solutions. The material domain $[0, \infty)$ is used throughout the computation procedure is condensed to the limited area $[\eta_0, \eta_\infty]$ by altering $\eta_0 = 0$, $\eta_\infty = 20$, $\eta_p = 1,000$ and $h = \dfrac{\eta_\infty - \eta_0}{\eta_p}$ to establish the initial approximations of the computerised solution, and subsequently increasing the total amount of points on the grid by decreasing the step size h to attain the necessary precision, i.e. ε^{-6}. We therefore present a more detailed exposition here. Essentially there are four fundamental steps intrinsic to the Keller box scheme. The Keller Box Method has several advantages other numerical methods for solving differential equations. Some of them are:

It can deal with complex boundary conditions such as mixed or nonlinear ones. it can achieve high accuracy and stability with relatively few boxes and it can be easily implemented on computers using simple algorithm.

Steps involved in this method is explained in detail below:

(A). Reduction of the Nth order partial differential equation system to N 1st order equations.

(B). Finite Difference Discretization.

(C). Quasi-linearization of Non-Linear Keller Algebraic Equations.

(D). Block-tridiagonal Elimination of Linear Keller Algebraic Equations.

Steps involved in this method is explained in detail below:

Step A: The Nth order partial differential equation system reduced to N first-order equations.

We add the most recent set of variables listed below to convert higher-order PDEs to first-order PDEs: $p_1(\xi, \eta)$, $p_2(\xi, \eta)$, $p_3(\xi, \eta)$, $p_4(\xi, \eta)$, $p_5(\xi, \eta)$.

$$f = f, \ f' = P_1, \ P_1' = f'' = P_2, \ f''' = P_2',$$

$$\theta = P_3, \ P_3' = \theta' = P_4, \ \theta'' = P_4',$$

$$g = g, \ g' = P_5, \ g'' = P_6, \ g''' = P_6'. \tag{19}$$

$$A_1\left(P_2'\right)-\left(P_1\right)^2+\left(f+g\right)P_2-S\left(P_1+\frac{\eta}{2}\left(P_2\right)\right)-A_2M\left(P_1\right)=0 \tag{20}$$

$$A_1\left(P_6'\right)-\left(P_5\right)^2+\left(f+g\right)\left(P_6\right)-S\left(P_5+\frac{\eta}{2}\left(P_6\right)\right)-A_2M\left(P_5\right)=0 \tag{21}$$

$$A_3\left(P_4'\right)\left(1+\frac{4}{3F}\right)+\Pr\left(\begin{array}{l}\left(f+g\right)\left(P_4\right)-\left(r\left(P_1\right)+s\left(P_5\right)\right)\left(P_3\right)\\-S\left(\left(P_3\right)+\frac{\eta}{2}\left(P_4\right)\right)+A_3\left(A\left(P_1\right)+B\left(P_3\right)\right)\end{array}\right)=0 \tag{22}$$

Boundary conditions

$$f\left(0\right)+g\left(0\right)=0,\ P_1\left(0\right)=1,\ P_5\left(0\right)=\alpha$$

$$P_4\left(0\right)=-Bi\left(1-\theta\left(0\right)\right),\ \text{at}\ \eta\to0$$

$$P_1\left(0\right)\to0,\ P_5\left(0\right)\to0,\ \theta\left(0\right)\to0\ \text{as}\ \eta\to\infty \tag{23}$$

Step B: The Finite Difference Method

The rectangular net is created whose net points are as follows:

$$\zeta^0=0,\ \zeta^i=\zeta^{i-1}+k_i,\ i=1,\ 2,\ 3,\ \ldots,\ I$$

$$\eta_0=0,\ \eta_j=\eta_{j-1}+h_j,\ j=1,\ 2,\ 3,\ \ldots,\ J \tag{24}$$

Where k_n and h_j represent the $\Delta\zeta$ and $\Delta\eta$ spacing, respectively.

$$\left(\frac{\partial(\ )}{\partial\zeta}\right)_{j-1/2}^{i-\frac{1}{2}}=\frac{(\ )_{j-\frac{1}{2}}^i-(\ )_{j-\frac{1}{2}}^{i-1}}{k_i} \tag{25}$$

$$\left(\frac{\partial(\ )}{\partial\eta}\right)_{j-1/2}^{i-\frac{1}{2}}=\frac{(\ )_{j-\frac{1}{2}}^i-(\ )_{j-\frac{1}{2}}^{i-1}}{h_j} \tag{26}$$

$$(\ )^{i-\frac{1}{2}}=\frac{(\ )_j^{i-1}-(\ )_j^i}{2},\ (\ )_{j-\frac{1}{2}}^i=\frac{(\ )_{j-1}^i-(\ )_j^i}{2} \tag{27}$$

The finite-difference form is computed using the central difference technique.

$$f' = P_1 \Rightarrow (P_1)^i_{j-\frac{1}{2}} = \frac{(P_1)^i_j + (P_1)^i_{j-1}}{2} = \frac{\left(f^i_j - f^i_{j-1}\right)}{h_j} \tag{28}$$

$$(P_1)' = P_2 \Rightarrow (P_2)^i_{j-\frac{1}{2}} = \frac{(P_2)^i_j + (P_2)^i_{j-1}}{2} = \frac{\left((P_1)^i_j - (P_1)^i_{j-1}\right)}{h_j} \tag{29}$$

$$(P_3)' = P_4 \Rightarrow (P_4)^i_{j-\frac{1}{2}} = \frac{(P_4)^i_j + (P_4)^i_{j-1}}{2} = \frac{\left((P_3)^i_j - (P_3)^i_{j-1}\right)}{h_j} \tag{30}$$

$$(P_4)' = P_5 \Rightarrow (P_5)^i_{j-\frac{1}{2}} = \frac{(P_5)^i_j + (P_5)^i_{j-1}}{2} = \frac{\left((P_4)^i_j - (P_4)^i_{j-1}\right)}{h_j} \tag{31}$$

$$(P_5)' = P_6 \Rightarrow (P_6)^i_{j-\frac{1}{2}} = \frac{(P_6)^i_j + (P_6)^i_{j-1}}{2} = \frac{\left((P_5)^i_j - (P_5)^i_{j-1}\right)}{h_j} \tag{32}$$

The following equations (31-35) are centred at the $\left(\xi^{i-\frac{1}{2}}, \eta_{j-\frac{1}{2}} \right)$ locations, which are shown below

$$A_1 \left(\frac{(P_2)^i_j - (P_2)^i_{j-1}}{h_j} \right) + \left(f^i_{j-\frac{1}{2}} + g^i_{j-\frac{1}{2}} \right)(P_2)^i_{j-\frac{1}{2}} - \left((P_1)^i_{j-\frac{1}{2}} \right)^2 -$$

$$S\left((P_1)^i_{j-\frac{1}{2}} + \frac{\eta}{2} \left((P_6)^i_{j-\frac{1}{2}} \right) \right) - A_2 M \left((P_1)^i_{j-\frac{1}{2}} \right) = 0 \tag{33}$$

$$A_1 \left(\frac{(P_6)^i_j - (P_6)^i_{j-1}}{h_j} \right) + \left(f^i_{j-\frac{1}{2}} + g^i_{j-\frac{1}{2}} \right)(P_6)^i_{j-\frac{1}{2}} - \left((P_5)^i_{j-\frac{1}{2}} \right) +$$

$$S\left((P_5)^i_{j-\frac{1}{2}} + \frac{\eta}{2}(P_6)^i_{j-\frac{1}{2}} \right) - A_2 M \left((P_5)^i_{j-1} \right) = 0 \tag{34}$$

$$A_3 = \left(\frac{\left(P_4 \right)_j^i - \left(P_4 \right)_{j-1}^i}{h_j} \right) \left(1 + \frac{4}{3F} \right) \frac{1}{\text{Pr}} + \left(f_{j-\frac{1}{2}}^i + g_{j-\frac{1}{2}}^i \right) \left(P_4 \right)_{j-\frac{1}{2}}^i - \left(r \left(P_1 \right)_{j-\frac{1}{2}}^i + s \left(P_5 \right)_{j-\frac{1}{2}}^i \right) \left(P_3 \right)_{j-\frac{1}{2}}^i$$

$$-S \left(\left(P_3 \right)_{j-\frac{1}{2}}^i + \frac{\eta}{2} \left(P_3 \right)_{j-\frac{1}{2}}^i \right) + A_3 \left(A \left(P_1 \right)_{j-\frac{1}{2}}^i + B \left(P_3 \right)_{j-\frac{1}{2}}^i \right) = 0 \tag{35}$$

Boundary conditions are

$$f_0^i = 0, \; g_0^i = 0, \; \left(P_1 \right)_0^i = 1, \; \left(P_5 \right)_0^i = \alpha$$

$$\left(P_4 \right)_0^i = -Bi \left(1 - \theta_0 \right)$$

$$\left(P_1 \right)_J^i = 0, \; \left(P_5 \right)_J^i = 0, \; \left(\theta \right)_J^i = 0. \tag{36}$$

Step C: Newton's linearization approach

Using well-known techniques $\left(f_j^{n-1}, \left(p_1 \right)_j^{n-1}, \left(p_2 \right)_j^{n-1}, \left(p_3 \right)_j^{n-1}, \left(p_4 \right)_j^{n-1}, \left(p_5 \right)_j^{n-1}, \ldots \right)$, the unknown $\left(f_j^n, \left(p_1 \right)_j^n, \right.$
$\left. \left(p_2 \right)_j^n, \left(p_3 \right)_j^n, \left(p_4 \right)_j^n, \left(p_5 \right)_j^n, \ldots \right)$ are predicted to be $0 \le j \le J$.

$$\left(f_j^n, \left(p_1 \right)_j^n, \left(p_2 \right)_j^n, \left(p_3 \right)_j^n, \left(p_4 \right)_j^n \ldots \right) \equiv \left(f_j, \left(p_1 \right)_j, \left(p_2 \right)_j, \left(p_3 \right)_j, \left(p_4 \right)_j \ldots \right). \tag{37}$$

The collection of Equations of central difference is denoted as

$$\frac{\left(P_1 \right)_j + \left(P_1 \right)_{j-1}}{2} = \frac{f_j - f_{j-1}}{h_j} \tag{38}$$

$$\frac{\left(P_2 \right)_j + \left(P_2 \right)_{j-1}}{2} = \frac{\left(P_1 \right)_j + \left(P_1 \right)_{j-1}}{h_j} \tag{39}$$

$$\frac{\left(P_4 \right)_j + \left(P_4 \right)_{j-1}}{2} = \frac{\left(P_3 \right)_j + \left(P_3 \right)_{j-1}}{h_j} \tag{40}$$

$$\frac{\left(P_6 \right)_j + \left(P_6 \right)_{j-1}}{2} = \frac{\left(P_5 \right)_j + \left(P_5 \right)_{j-1}}{h_j} \tag{41}$$

$$A_1\left((P_2)_j - (P_2)_{j-1}\right) + h_j\left(\left(f_{j-\frac{1}{2}} + g_{j-\frac{1}{2}}\right)(P_2)_{j-\frac{1}{2}} - S\left((P_1)_{j-\frac{1}{2}} + \frac{\eta}{2}(P_6)_{j-\frac{1}{2}}\right)\right.$$

$$-(P_1)^2_{j-\frac{1}{2}} - A_2 M (P_1)_{j-\frac{1}{2}} = 0 \tag{42}$$

$$A_1\left((P_6)_j - (P_6)_{j-1}\right) + h_j\left(\left(f_{j-\frac{1}{2}} + g_{j-\frac{1}{2}}\right)(P_6)_{j-\frac{1}{2}} - S\left((P_5)_{j-\frac{1}{2}} + \frac{\eta}{2}(P_6)_{j-\frac{1}{2}}\right)\right.$$

$$-(P_5)^2_{j-\frac{1}{2}} - A_2 M (P_5)_{j-\frac{1}{2}} = 0 \tag{43}$$

$$A_1\left((P_4)_j - (P_4)_{j-1}\right)\left(1 + \frac{4}{3F}\right) + h_j\,\mathrm{Pr}\left(\left(f_{j-\frac{1}{2}} + g_{j-\frac{1}{2}}\right)(P_4)_{j-\frac{1}{2}} - S\left((P_3)_{j-\frac{1}{2}} + \frac{\eta}{2}(P_3)_{j-\frac{1}{2}}\right)\right.$$

$$-\left(r(P_1)_{j-\frac{1}{2}} + s(P_5)_{j-\frac{1}{2}}\right)(P_3)_{j-\frac{1}{2}} + A_3\left(A^*(P_1)_{j-\frac{1}{2}} + B^*(P_3)_{j-\frac{1}{2}}\right) = 0 \tag{44}$$

We present the iterates below to use Newton's method to convert to a nonlinear collection of equations approach.

$$\Delta f_j^{(n)} \quad + \quad f_j^n \quad = \quad f_j^{(n+1)}$$

$$\Delta (p_1)_j^{(n)} \quad + \quad (p_1)_j^{(n)} \quad = \quad (p_1)_j^{(n+1)}$$

$$\Delta (p_2)_j^{(n)} \quad + \quad (p_2)_j^{(n)} \quad = \quad (p_2)_j^{(n+1)}$$

$$\Delta (p_3)_j^{(n)} \quad + \quad (p_3)_j^{(n)} \quad = \quad (p_3)_j^{(n+1)}$$

$$\Delta (p_4)_j^{(n)} \quad + \quad (p_4)_j^{(n)} \quad = \quad (p_4)_j^{(n+1)}$$

$$\Delta (p_5)_j^{(n)} \quad + \quad (p_5)_j^{(n)} \quad = \quad (p_5)_j^{(n+1)}$$

$$\Delta (p_6)_j^{(n)} \quad + \quad (p_6)_j^{(n)} \quad = \quad (p_6)_j^{(n+1)}$$

This method results in the following linear system (the superscript (n) has been deleted for clarity).

$$\Delta f_j - \Delta f_{j-1} - \frac{h_j}{2}\Delta(p_1)_j - \frac{h_j}{2}\Delta(p_1)_{j-1} - (l_1)_j = 0 \tag{45}$$

$$\Delta(p_1)_j - \Delta(p_1)_{j-1} - \frac{h_j}{2}\Delta(p_2)_j - \frac{h_j}{2}\Delta(p_2)_{j-1} - (l_2)_j = 0 \tag{46}$$

$$\Delta(p_3)_j - \Delta(p_3)_{j-1} - \frac{h_j}{2}\Delta(p_4)_j - \frac{h_j}{2}\Delta(p_4)_{j-1} - (l_3)_j = 0 \tag{47}$$

$$\Delta(p_5)_j - \Delta(p_5)_{j-1} - \frac{h_j}{2}\Delta(p_6)_j - \frac{h_j}{2}\Delta(p_6)_{j-1} - (l_4)_j = 0 \tag{48}$$

$$(G_1)_j \Delta(p_2)_j + (G_2)_j \Delta(p_2)_{j-1} + (G_3)_j \Delta f_j + (G_4)_j \Delta f_{j-1} + (G_5)_j \Delta(p_1)_j +$$

$$(G_6)_j \Delta(p_1)_{j-1} + (G_7)_j \Delta(p_3)_j + (G_8)_j \Delta(p_3)_{j-1} - (l_5)_j = 0 \tag{49}$$

$$(H_1)_j \Delta(p_6)_j + (H_2)_j \Delta(p_6)_{j-1} + (H_3)_j \Delta(f_j) + (H_4)_j \Delta(f_{j-1}) + (H_5)_j \Delta(g)_j +$$

$$(H_6)_j \Delta(g)_{j-1} + (H_7)_j \Delta(p_5)_j + (H_8)_j \Delta(p_5)_{j-1} - (l_6)_j = 0 \tag{50}$$

$$(I_1)_j \Delta(P_4)_j + (I_2)_j \Delta(P_4)_{j-1} + (I_3)_j \Delta(f_j) + (I_4)_j \Delta(f_{j-1}) + (I_5)_j \Delta(g_j) +$$

$$(I_6)_j \Delta(g_{j-1}) + (I_7)_j \Delta(P_3)_j + (I_8)_j \Delta(P_3)_{j-1} + (I_9)_j \Delta(P_1)_j +$$

$$(I_{10})_j \Delta(P_1)_{j-1} + (I_{11})_j \Delta(P_5)_j + (I_{12})_j \Delta(P_5)_{j-1} - (l_7) = 0 \tag{51}$$

Where:

$$(G_1)_j = A_1 + \frac{h_j}{2}\left((f)_{j-\frac{1}{2}} + (g)_{j-\frac{1}{2}}\right) - \frac{h_j}{2} * S * \frac{\eta}{2}$$

$$(G_2)_j = -A_1 + \frac{h_j}{2}\left((f)_{j-\frac{1}{2}} + (g)_{j-\frac{1}{2}}\right) - \frac{h_j}{2} * S * \frac{\eta}{2}$$

$$(G_3)_j = \frac{h_j}{2} * (P_3)_{j-\frac{1}{2}}$$

$$(G_4)_j = \frac{h_j}{2} * (P_3)_{j-\frac{1}{2}}$$

$$(G_5) = -h_j * \left(P_{j-\frac{1}{2}} \right) - S * \frac{h_j}{2} - A_2 * \frac{h_j}{2} * M^2$$

$$(G_6) = -h_j * \left(P_{j-\frac{1}{2}} \right) - S * \frac{h_j}{2} - A_2 * \frac{h_j}{2} * M^2$$

$$(G_7) = \frac{h_j}{2} * (P_3)_{j-\frac{1}{2}}$$

$$(G_8) = \frac{h_j}{2} * (P_3)_{j-\frac{1}{2}}$$

$$(H_1) = A_1 + \frac{h_j}{2} * \left(f_{j-\frac{1}{2}} + g_{j-\frac{1}{2}} \right) - \left(S * \frac{\eta}{4} \right)$$

$$(H_2) = A_1 + \frac{h_j}{2} * \left(f_{j-\frac{1}{2}} + g_{j-\frac{1}{2}} \right) - \left(S * \frac{\eta}{4} \right)$$

$$(H_3) = -h_j * (P_5)_{j-\frac{1}{2}} - S * \frac{h_j}{2} - \frac{h_j}{2} * A_2 * M^2$$

$$(H_4) = -h_j * (P_5)_{j-\frac{1}{2}} - S * \frac{h_j}{2} - \frac{h_j}{2} * A_2 * M^2$$

$$(H_5)_j = \frac{h_j}{2} * u_{j-\frac{1}{2}}$$

$$(H_6)_j = \frac{h_j}{2} * u_{j-\frac{1}{2}}$$

$$(H_7)_j = \frac{h_j}{2} * u_{j-\frac{1}{2}}$$

$$(H_8)_j = \frac{h_j}{2} * u_{j-\frac{1}{2}}$$

$$(I_1)_j = A_3 * \left(1 + \frac{4}{3F}\right) + \frac{h_j}{2}\text{Pr}\left(f_{j-\frac{1}{2}} + g_{j-\frac{1}{2}}\right) - \frac{h_j}{2} * \text{Pr} * \frac{\eta}{2} * S$$

$$(I_2)_j = -A_3 * \left(1 + \frac{4}{3F}\right) + \frac{h_j}{2}\text{Pr}\left(f_{j-\frac{1}{2}} + g_{j-\frac{1}{2}}\right) - \frac{h_j}{2} * \text{Pr} * \frac{\eta}{2} * S$$

$$(I_3)_j = \frac{h_j}{2} * \text{Pr} * (P_4)_{j-\frac{1}{2}} + A^* \frac{h_j}{2} * A_3 * \text{Pr}$$

$$(I_4)_j = \frac{h_j}{2} * \text{Pr} * (P_4)_{j-\frac{1}{2}} + A^* \frac{h_j}{2} * A_3 * \text{Pr}$$

$$(I_5)_j = \frac{h_j}{2} * \text{Pr} * (P_4)_{j-\frac{1}{2}}$$

$$(I_6)_j = \frac{h_j}{2} * \text{Pr} * (P_4)_{j-\frac{1}{2}}$$

$$(I_7)_j = -r * \frac{h_j}{2} * \text{Pr} * (P_3)_{j-\frac{1}{2}} + B^* * A_3 * \frac{h_j}{2} * \text{Pr}$$

$$(I_8)_j = -r * \frac{h_j}{2} * \text{Pr} * (P_3)_{j-\frac{1}{2}} + B^* * A_3 * \frac{h_j}{2} * \text{Pr}$$

$$(I_9)_j = -s * \frac{h_j}{2} * \text{Pr} * (P_3)_{j-\frac{1}{2}}$$

$$(I_{10})_j = -s * \frac{h_j}{2} * \text{Pr} * (P_3)_{j-\frac{1}{2}}$$

$$(I_{11})_j = -\frac{h_j}{2} * \text{Pr} * \left(r * P_{j-\frac{1}{2}} + s * (P_4)_{j-\frac{1}{2}}\right) - \frac{h_j}{2} * \text{Pr} * S$$

$$(I_{12})_j = -\frac{h_j}{2} * \text{Pr} * \left(r * P_{j-\frac{1}{2}} + s * (P_4)_{j-\frac{1}{2}}\right) - \frac{h_j}{2} * \text{Pr} * S$$

With the boundary conditions

$$\Delta f_0 = 0,\ \Delta g_0 = 0,\ \Delta (P_1)_0 = 0,\ \Delta (P_5)_0 = 0,$$

$$\Delta\left(P_4\right)_0 = Bi\Delta\theta_0 \text{ at } \eta = 0,$$

$$\Delta\left(P_1\right)_J = 0, \ \Delta\left(P_5\right)_J = 0, \ \Delta\left(\theta\right)_J = 0 \text{ as } \eta \to \infty. \tag{52}$$

Step D: Block-tridiagonal Elimination of Linear Keller Algebraic Equations.

The block-elimination approach may be used to solve the linearized difference Eqn. (45)-(52) by Cebeci and Bradshaw, because the system is block-tridiagonal in structure. The block-tridiagonal structure is often made up of variables or constants, but in this case, an unusual aspect is that it is made up of block matrices, Eqn. (45)-(52) may be represented in matrix-vector form as

$$Q\Omega = l \tag{53}$$

Where:

$$Q = \begin{bmatrix} [Q_1] & [R_1] & & & & \\ [R_2] & [Q_2] & [S_2] & \cdot & & \\ & & & \cdot & & \\ & & & & \cdot & \\ & & & [R_{j-1}] & [Q_{j-1}] & [S_{j-1}] \\ & & & & [R_j] & [Q_j] \end{bmatrix}$$

$$\Omega = \begin{bmatrix} [\Omega_1] \\ [\Omega_2] \\ \cdot \\ \cdot \\ \cdot \\ [\Omega_{j-1}] \\ [\Omega_j] \end{bmatrix} \quad \text{and} \quad l = \begin{bmatrix} [l_1] \\ [l_2] \\ \cdot \\ \cdot \\ \cdot \\ [l_{j-1}] \\ [l_j] \end{bmatrix}$$

The matrix components the following.
Where:

$$-\frac{h_j}{2} = -z$$

$$[Q_1] = \begin{bmatrix} 0 & 0 & 0 & 1 & 0 & 0 & 0 & 0 \\ -z & 0 & 0 & 0 & 0 & -z & 0 & 0 \\ 0 & 0 & 0 & 0 & 1 & 0 & 0 & 0 \\ 0 & -1 & 0 & 0 & 0 & 0 & -z & 0 \\ 0 & 0 & -z & 0 & 0 & 0 & 0 & -z \\ G_2 & 0 & 0 & G_3 & G_7 & G_1 & 0 & 0 \\ 0 & H_2 & 0 & H_5 & H_7 & 0 & H_1 & 0 \\ 0 & 0 & C_2 & C_3 & C_5 & 0 & 0 & C_1 \end{bmatrix}, \quad [Q_j] = \begin{bmatrix} -z & 0 & 0 & 1 & 0 & 0 & 0 & 0 \\ -1 & 0 & 0 & 0 & 0 & -z & 0 & 0 \\ 0 & -z & 0 & 0 & 1 & 0 & 0 & 0 \\ 0 & -1 & 0 & 0 & 0 & 0 & -z & 0 \\ 0 & 0 & -z & 0 & 0 & 0 & 0 & -z \\ G_2 & 0 & 0 & G_3 & G_7 & G_1 & 0 & 0 \\ 0 & H_4 & 0 & H_5 & H_7 & 0 & H_1 & 0 \\ C_8 & C_{10} & C_{12} & C_3 & C_5 & 0 & 0 & C_1 \end{bmatrix}$$

$$[R_j] = \begin{bmatrix} 0 & 0 & 0 & -1 & 0 & 0 & 0 & 0 \\ 0 & 0 & 0 & 0 & 0 & -z & 0 & 0 \\ 0 & 0 & 0 & 0 & -1 & 0 & 0 & 0 \\ 0 & 0 & 0 & 0 & 0 & 0 & -z & 0 \\ 0 & 0 & 0 & 0 & 0 & 0 & 0 & -z \\ 0 & 0 & 0 & G_4 & G_8 & G_2 & 0 & 0 \\ 0 & 0 & 0 & H_6 & H_8 & 0 & H_2 & 0 \\ 0 & 0 & 0 & C_4 & C_6 & 0 & 0 & C_2 \end{bmatrix}, \quad [S_j] = \begin{bmatrix} -z & 0 & 0 & 0 & 0 & 0 & 0 & 0 \\ 1 & 0 & 0 & 0 & 0 & 0 & 0 & 0 \\ 0 & -z & 0 & 0 & 0 & 0 & 0 & 0 \\ 0 & 1 & 0 & 0 & 0 & 0 & 0 & 0 \\ 0 & 0 & 1 & 0 & 0 & 0 & 0 & 0 \\ G_5 & 0 & 0 & 0 & 0 & 0 & 0 & 0 \\ 0 & H_3 & 0 & 0 & 0 & 0 & 0 & 0 \\ C_7 & C_9 & C_{11} & 0 & 0 & 0 & 0 & 0 \end{bmatrix}$$

For the category $J \geq j \geq 2$:

$$[\Delta_1] = \begin{bmatrix} \Delta(P_4)_0 \; \Delta(P_3)_0 \; \Delta(P_2)_0 \; \Delta(P_5)_0 \; \Delta f_1 \Delta(P_4)_1 \; \Delta(P_4)_1 \; \Delta(P_4)_1 \end{bmatrix}^T$$

for $2 \leq j \leq J$,

$$[\Delta_j] = \begin{bmatrix} \Delta(P_4)_{j-1} \; \Delta(P_3)_{j-1} \; \Delta(P_2)_{j-1} \; \Delta(P_5)_j \; \Delta f_j \Delta(P_4)_j \; \Delta(P_4)_j \; \Delta(P_4)_j \end{bmatrix}^T$$

for $1 \leq j \leq J$,

$$[l_j] = \begin{bmatrix} (l_1)_{j-\frac{1}{2}} \\ (l_2)_{j-\frac{1}{2}} \\ (l_3)_{j-\frac{1}{2}} \\ (l_4)_{j-\frac{1}{2}} \\ (l_5)_{j-\frac{1}{2}} \\ (l_6)_{j-\frac{1}{2}} \\ (l_7)_{j-\frac{1}{2}} \\ (l_8)_{j-\frac{1}{2}} \end{bmatrix}$$

The *LU* decomposition technique may be used to find the solution of a tri-diagonal system. Assuming that matrix A is non-singular, it may be factored into the product of two matrices, denoted by the notation $A = LU$.

Where:

$$L = \begin{bmatrix} [a_1] & & & & \\ [b_1] & [a_2] & & & \\ & [b_3] & [a_3]... & & \\ & & & [b_{J-1}][a_{J-1}] & \\ & & & & [b_J] & [a_J] \end{bmatrix}, \quad U = \begin{bmatrix} [I_1] & [c_1] & & & \\ & [I_2] & [c_2] & & \\ & & ... & & \\ & & & [I_{J-1}] & [c_{J-1}] \\ & & & & [I_J] \end{bmatrix}$$

where $[a_j]$ and $[c_j]$ are (8 × 8) matrices, and $[I_J]$ is the (8 × 8) identity matrix. We may get the elements of these matrices using the following equations:

$$[A_1] = [a_1] \tag{54}$$

$$[A_j] = [b_j][c_j] + [a_j], \text{ for } j = 2, 3, ..., J \tag{55}$$

$$[C_j] = [a_j][c_j], \text{ for } j = 1, 2, 3, ..., J-1 \tag{56}$$

$$[B_j] = [b_j], \text{ for } j = 2, 3, 4, ..., J \tag{57}$$

Since $= LU$, the equation $A\Delta = l$ to the

$$LU\Delta = l \tag{58}$$

Let

$$U\Delta = Z \tag{59}$$

Then

$$LZ = l \tag{60}$$

Where:

$$Z = \begin{bmatrix} [Z_1] \\ [Z_1] \\ [Z_1] \\ . \\ . \\ . \\ [Z_{J-1}] \\ [Z_J] \end{bmatrix} \tag{61}$$

Form the equation (63) we get

$$[Z_1] = [a_1] \backslash [l_1] \tag{62}$$

$$[Z_j] = [a_j] \backslash ([l_1] - [b_j][Z_{j-1}]), \text{ for } 2 \le j \le j \tag{63}$$

Then, form equation (62) we get

$$[\Delta_j] = [Z_j] - [c_j][\Delta_{j+1}], \text{ for } 1 \le j \le j-1 \tag{64}$$

$$[\Delta_J] = [Z_J] \tag{65}$$

4. Validation of results

The new findings are compared with prior impressive research that demonstrated great agreement to corroborate Keller box approach, and this problem using to the tri-hybrid nanofluid with water as conducting fluid. The nanofluid, hybrid nanofluid and tri-hybrid nanoflow combinations. Table 2 describes the Keller box convergence for different grid points varying from [500, 2500]. Table 3 shows the corroboration table of our numerical computations (skin friction) with KBM and Liu & Andersson [34] with RKM, which shows a fine agreement.

Table 2. A grid-independent method to the Keller-Box solution of the current mathematical model when $\alpha = M = S = 0.5$, $r = s = 1.0$ and $\phi_1 = \phi_2 = \phi_3 = 0.05$

Grid point	$-f''(0)$	$-g''(0)$	$-\theta'(0)$
500	1.745074	0.811573	0.230769
1,000	1.778522	0.822983	0.230769
1,500	1.778623	0.823102	0.230769
2,000	1.779112	0.823112	0.230769
2,500	1.779113	0.823112	0.230769

Table 3. Thorough verification of the current outcomes with previous investigations when $\alpha = M = S = 0.5$, $r = s = 1.0$, $Bi = 0.3$ and $\phi_1 = \phi_2 = \phi_3 = 0$

α	Present (KBM) ($f''(0)$)	Published Liu and Andersson [33] (RKM) ($f''(0)$)	Present (KBM) ($g''(0)$)	Published (RKM) Liu and Andersson [33] ($g''(0)$)
0.00	1.0	1.0	0	0
0.25	1.047793	1.048813	0.194565	0.194565
0.50	1.089624	1.093096	0.465206	0.465206
0.75	1.127791	1.134486	0.794619	0.794619
1.00	1.163369	1.173721	1.163369	1.173721

5. Results and discussion

The influence of various factors on axial velocity (f), transverse velocity (g), temperature (θ), stretching parameter (α), unsteadiness parameter (S), thermal indices (r, s) and thermal conjugacy number (Bi) is displayed and briefly described. Table 1 lists the thermophysical characteristics of the materials in use. The findings of the current investigation were achieved for fixed values: $Pr = 6.2$, $S = 0.5$, $Bi = 0.3$, $\alpha = 0.5$, $r = 1.0$, $M = 0.5$, $s = 1.0$, $n_p = 2,500$, $\xi_{max} = 20$, $\phi_1 = 0.02$, $\phi_2 = 0.02$, $\phi_3 = 0.01$. The results are contrasted using the HNF($Fe_3O_4 + Ag/H_2O$) and THNF ($Fe_3O_4 + Ag + Al_2O_3/H_2O$). The leading boundary layer equations are solved using Thomas algorithm and numerical computations are carried with MATLAB software to show the impact of various pertinent physical parameters on the flow field and engineering quantities through Figures 2-23.

5.1 *Nanoflow momentum analysis*

Figures 2-3 show that the transverse velocity (g') and axial velocity (f') with varied M ($M = 0.5, 1.0, 1.5, 2.0$). Nanoflow momentum obstructs by induced Lorentzian forces as the strength of magnetic force is increased. Thus, momentum BL thins and the fluid velocity in both the axial and transverse directions decelerate. Figures 4-5 represent the axial and transverse momentum variations with different S ($S = 1.0, 5, 10, 15$), unsteadiness parameter. Expansion rates a' decreases with improving S values, which has a stronger effect on the behaviour of the system. As a result, the nanoflow motion slows down. Additionally, as S increases, the thickness of the boundary layer decreases as well.

Figures 6-7 portray how stretching force ratio (α) influences the nanoflow momentum. Augmenting α, decelerates the velocity along x direction whilst stretches more in y direction, accelerating the motion of the flow in both cases i.e., axial /transverse velocities increase for improving α. For $\alpha = 0$, the stretching happens along x axis. On the other hand, stretching along the x and y axes are equal when $\alpha = 1$. As a result, the momentum boundary layer representing the axial and transverse velocities coincides. It is evident that the degree of stretching along the surfaces y axis becomes more noticeable as a rise in contrast to the stretching along the x axis. Iron oxide and silver suspended water based hybrid nanoflow shows higher momentum rates than trihybrid nanofluids in all the physical parameter variations. But in the case of surface stretching ratio ternary nanoflow has dominant values than hybrid flows.

5.2 *Energy flow analysis*

Figure 8 depicts influence of variable magnetic force on the nanoflow energy. Energy profiles of the nanoflow enhances as the viscosity of the fluid reduces when exposed to magnetic force along z-axis. Physically, the boundary layer becomes hotter as a result of the augmentation of M resulting in a decrease in the amplitude of velocity profiles inside the boundary layer. It is seen that steadiness of the flow field is varied, the nanoflow energy profiles diminishes. The growth rate falls with increasing S magnitude, moreover, when the unsteady factor increases, the thickness of

the thermal boundary layer decreases (Figure 9). Figure 10 illustrate how the temperature changes for different α. As stretching ration improves, the temperature drops. The main cause of the thermal decrease is the dominance of expansion rates along the y axis over x axis. Figure 11 demonstrates the temperature for different values of Rd. When the fluid exposed to radiation, the internal heat of the fluid starts heating up. Physically, the boundary layer becomes hotter as a result of the augmentation of the Rd, which results in a decrease in the amplitude of velocity profiles inside the boundary layer. The temperature distribution as r and s fluctuate is seen in Figures 12-13. As r, ($r = 1.0, 2.0, 3.0, 4.0$) and s, ($s = 1.0, 2.0, 3.0, 4.0$) varies, the nanoflow temperature reduces. It is clear that sheet temperature non-uniformity affects temperature profiles; greater values of r and s lead to lower temperatures and thinner thermal boundary layers, respectively. Additionally, a larger temperature distribution is produced by negative r and s values than by positive r and s values. Figures 14-15 exhibit the temperature for different values of A, $B > 0$ which represents energy generation inside the fluid. As the energy generation parameter enhances, the temperature profiles are enhanced. The parameters A, B increased, the energy production improvises and thereby improving the BL thickness of energy. Here in the temperature distribution case, the iron oxide, silver, alumina immersed water-based trihybrid nanoflow has higher values that hybrid nanoflows.

Table 4. Skin friction values of a ternary hybrid nanofluid ($Fe_3O_4 + Ag + Al_2O_3$) and hybrid nanofluid ($Fe_3O_4 + Ag$) at different volume percentages of nanoparticles

Physical parameters with $\phi_1 = \phi_2 = \phi_3 = 0.05\%$	$-C_{fx}\, Re_x^{\frac{1}{2}}$ ($Fe_3O_4 + Ag + Al_2O_3$)	$-C_{fy}\, Re_y^{\frac{1}{2}}$ ($Fe_3O_4 + Ag + Al_2O_3$)	$-C_{fx}\, Re_x^{\frac{1}{2}}$ ($Fe_3O_4 + Ag$)	$-C_{fy}\, Re_y^{\frac{1}{2}}$ ($Fe_3O_4 + Ag$)
$M = 0.5$	2.018226597	0.935870847	2.016346487	0.935870847
$M = 1.0$	2.293835013	1.065012791	2.182713025	1.045011782
$M = 1.5$	2.680477067	1.288335757	2.460477082	1.165335236
$\alpha = 0$	2.413036831	0.000000000	2.213026641	0.000000000
$\alpha = 0.5$	2.018222659	0.935870847	2.002587369	0.935870847
$\alpha = 1.0$	1.687907702	1.687907702	1.576804504	1.568906852
$S = 0$	1.871738528	0.856957265	1.648654879	0.756842541
$S = 0.5$	2.018226597	0.935870847	2.002587642	0.863254124
$S = 1.0$	2.161194031	1.012640693	2.024638924	1.002554884
$A = 0.1$	2.156456213	1.235689425	2.025469752	1.014568752
$A = 0.2$	2.165894251	1.248657825	2.023658742	1.024586521
$A = 0.3$	2.166789524	1.268456789	2.056321785	1.124563878

Table 4 describes the skin friction values of a ternary hybrid nanofluid ($Fe_3O_4 + Ag + Al_2O_3$) and ($Fe_3O_4 + Ag$) at different volume percentages of nanoparticles and different values of M, S, α, A, Bi. Axial wall drag coefficient seems higher than transverse direction ie., the friction force along x-axis is higher than y-axis. Stretching ratio velocity accelerates along axial direction whereas the transversal friction decelerates. Variable magnetic application decreases the skin friction coefficient values. Unsteadiness ratio also increments the wall shear stresses. Energy generation

improvisation also increments the coefficient of axial and transverse drag friction.

Table 5. The heat transfer rate and Nusselt number of the nanofluids for different $\phi_1\phi_2\phi_3$ values $(Nu_x\,\mathrm{Re}_x^{-1/2})$

$\phi_1\phi_2\phi_3$ ($\phi_1=\phi_2=\phi_3$ = 0.05%)	Fe_3O_4 ($\phi_2\phi_3$= 0) $(Nu_x\,\mathrm{Re}_x^{-1/2})$	$(E_R\%)$ heat transfer rate Estimated error	Ag ($\phi_1\phi_3$= 0) $(Nu_x\,\mathrm{Re}_x^{-1/2})$	$(E_R\%)$ heat transfer rate Estimated error	Al_2O_3 ($\phi_1\phi_3$= 0) $(Nu_x\,\mathrm{Re}_x^{-1/2})$	$(E_R\%)$ heat transfer rate Estimated error
0.00	3.789531	0%	3.789531	0%	3.789531	0%
0.01	3.181376	0.63%	3.814163	0.64%	3.815682	0.65%
0.02	3.837762	1.27%	3.838547	1.29%	3.848685	1.31%
0.03	3.885042	2.52%	3.886526	2.55%	3.894624	2.57%
0.04	3.931395	3.47%	3.933440	3.79%	3.956431	3.81%
0.05	3.976798	4.94%	3.979256	5.00%	3.984252	5.02%

Table 6. The heat transfer rate and Nusselt number of the nanofluids for different $\phi_1\phi_2\phi_3$ values of $(Nu_y\,\mathrm{Re}_y^{-1/2})$

$\phi_1\phi_2\phi_3$ ($\phi_1=\phi_2=\phi_3$ = 0.05%)	Fe_3O_4 ($\phi_2\phi_3$= 0) $(Nu_y\,\mathrm{Re}_y^{-1/2})$	$(E_R\%)$ heat transfer rate Estimated error	Ag ($\phi_1\phi_3$= 0) $(Nu_y\,\mathrm{Re}_y^{-1/2})$	$(E_R\%)$ heat transfer rate Estimated error	Al_2O_3 ($\phi_1\phi_3$= 0) $(Nu_y\,\mathrm{Re}_y^{-1/2})$	$(E_R\%)$ heat transfer rate Estimated error
0.00	3.789531	0%	3.789531	0%	3.789531	0%
0.01	3.182453	0.64%	3.826582	0.65%	3.815762	0.66%
0.02	3.849864	1.28%	3.846675	1.31%	3.848786	1.32%
0.04	3.892563	2.53%	3.893562	2.57%	3.894762	2.59%
0.05	3.942564	3.48%	3.946325	3.81%	3.956464	3.83%
0.06	3.986452	4.96%	3.987624	5.02%	3.987346	5.05%

Tables 5-6 illustrate the local energy transfer rates of the nanoflow along $x-y$ directions for different $\phi_1\phi_2\phi_3$ values $(Nu_x\,\mathrm{Re}_x^{-1/2})$. The error estimation also shown in tables. As the NPs volume fractions improves, the energy transmission rate of iron oxide nanoflow increases $0.01 \leq \phi_1\phi_2\phi_3 \leq 0.06$. Similar trend is observed for silver nanofluid and alumina nanofluid. When $\phi_1\phi_2\phi_3 = 0$, ie., viscous flow case heat transfer rate is higher and same in iron and aluminium oxides whereas for silver, the value is less. It shows that metal oxides transfer more heat from the system than that of metals (Table 4). The estimated error of heat transfer rate is higher in alumina nanoflow followed by silver and iron oxide nanofluid flows.
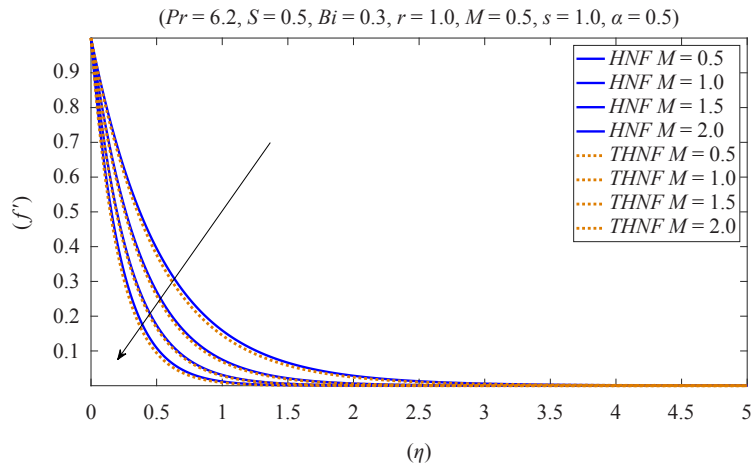
Figure 2. Variation of velocity (f') for various value of M
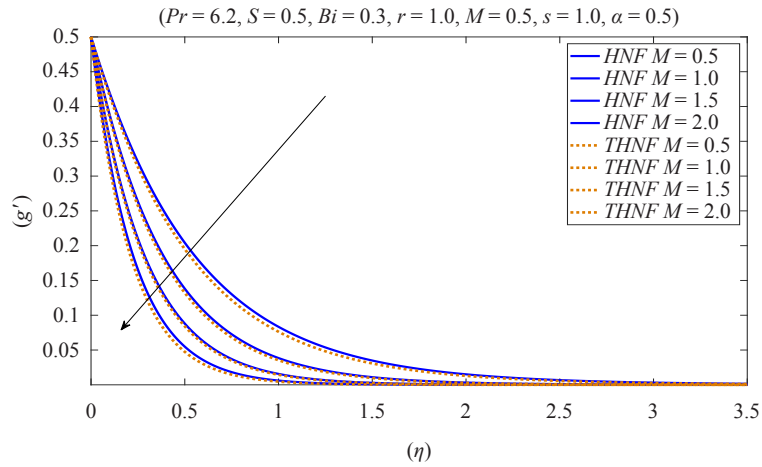
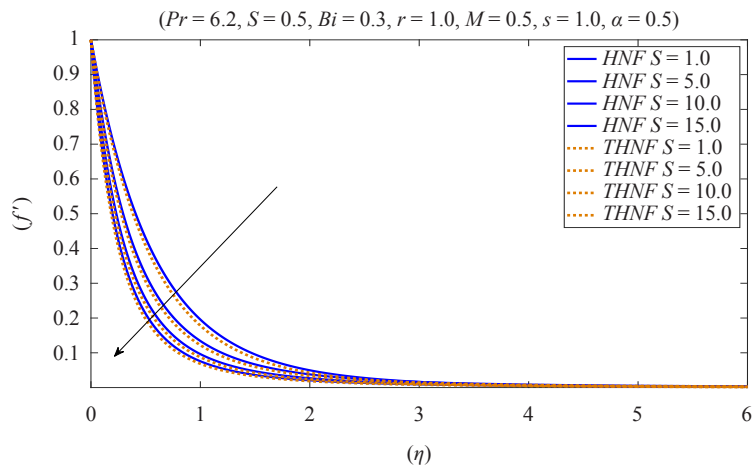**Figure 3.** Variation of velocity (g') for various value of M

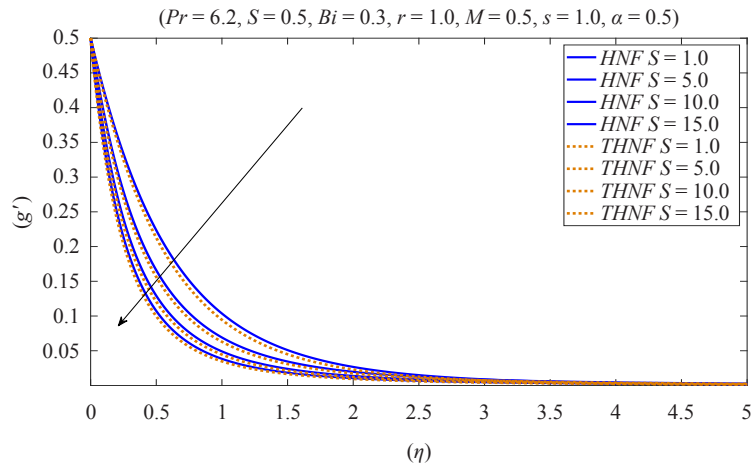**Figure 4.** Variation of velocity (f') for various value of S

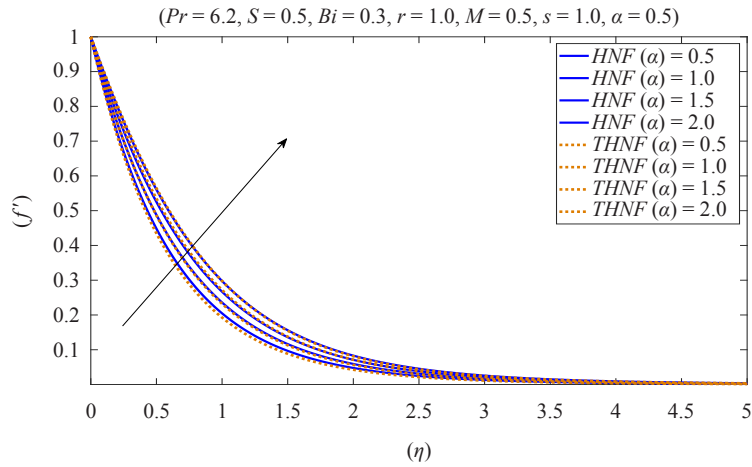**Figure 5.** Variation of velocity (g') for various value of S

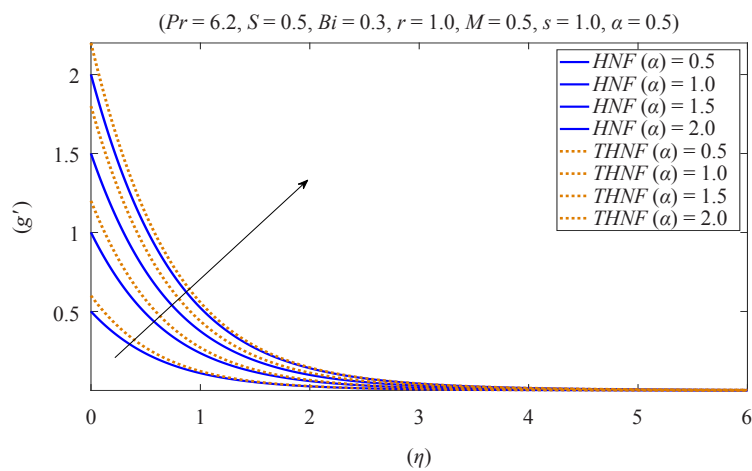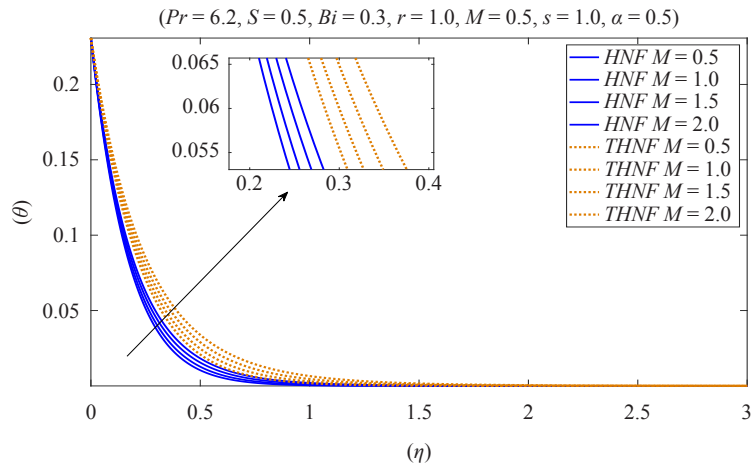**Figure 6.** Variation of velocity (f') for various value of α

Figure 7. Variation of velocity (g') for various value of α

Figure 8. Variation of temperature (θ) for various value of M
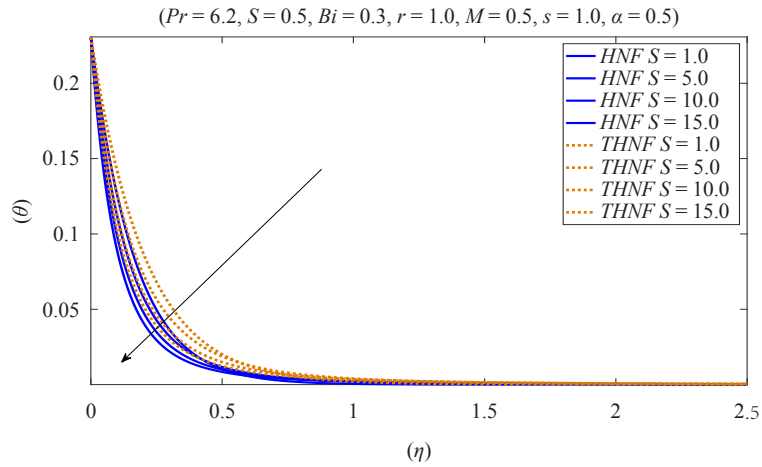
Figure 9. Variation of temperature (θ) for various value of S
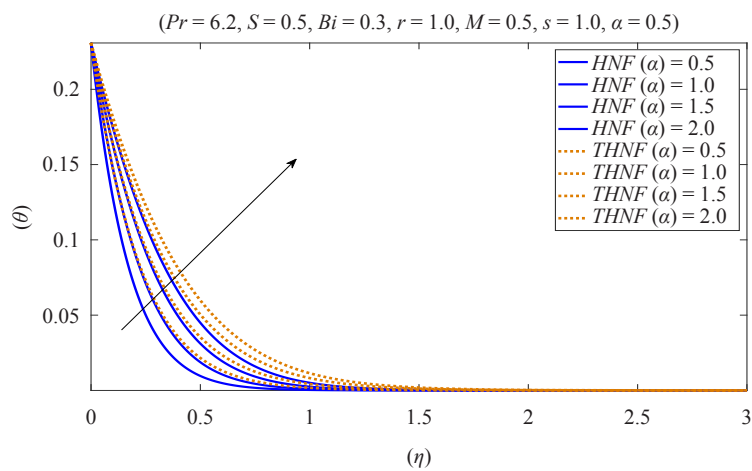
Figure 10. Variation temperature of (θ) for various value of (α)
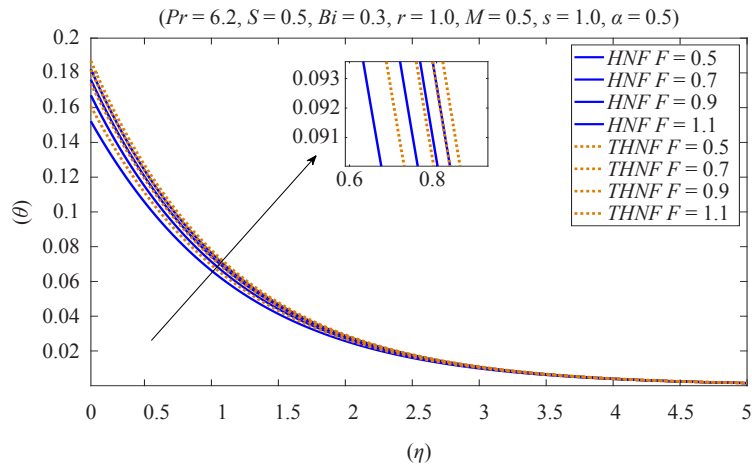
Figure 11. Variation of temperature (θ) for various value of F
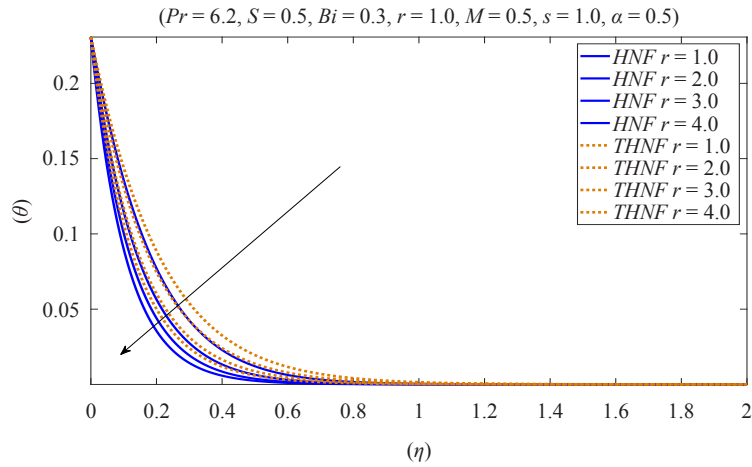
Figure 12. Variation temperature of (θ) for various value of r
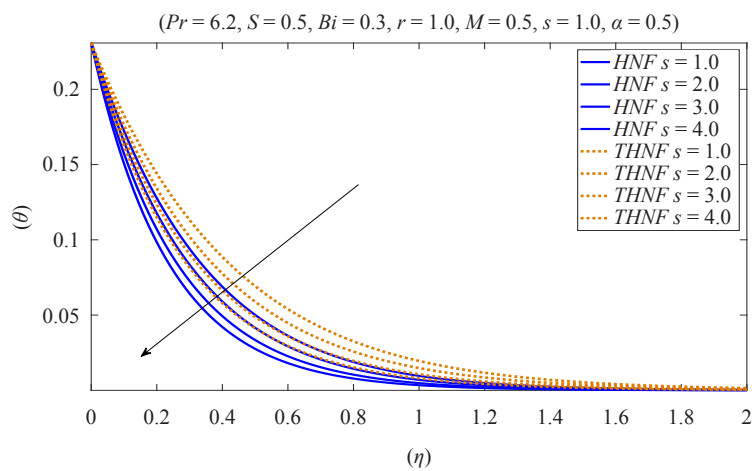
Figure 13. Variation of temperature (θ) for various value of s
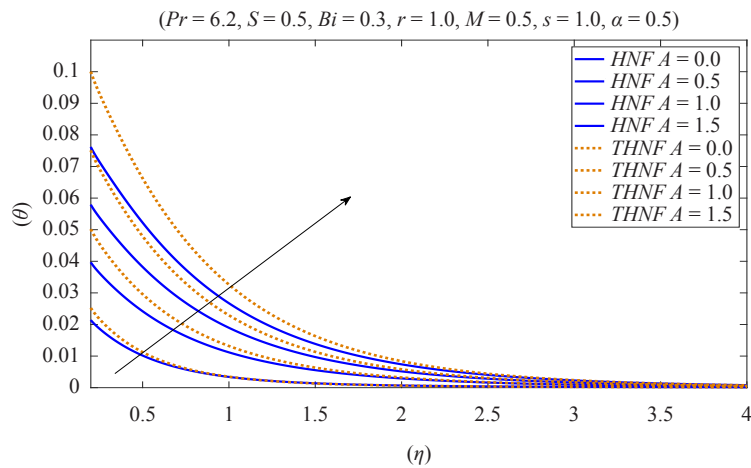
Figure 14. Variation of temperature (θ) for various value of A
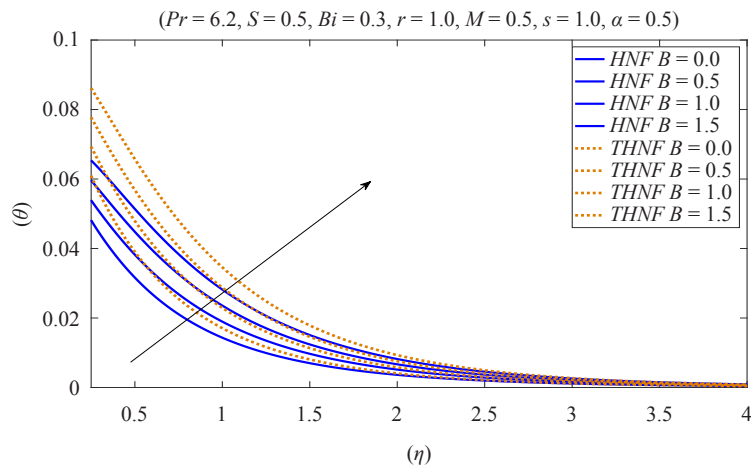
Figure 15. Variation of temperature (θ) for various value of B

Figures 16-23 exhibit the streamlines for Fe_3O_4 (33%) + Ag (33%) + Al_2O_3 (33%) ternary hybrid nanofluids. These level curve represents the intensity of the stream lines. Figures 16-17 show the streamlines for M (M = 1.0, and 2.0) the starting and ending points (M = 1.0) 0.94804 to 13.2725, the difference between each set of streamlines is same 0.948 and for M = 2.0, 0.816 the streamlines difference for M = 1.0 is higher than M = 2.0. The streamlines are equally spaced but the energy flow amount is higher in M = 1 than M = 2. Similar trend is observed for unsteadiness parameter too i.e., the streamline difference in S = 1 (is 1.02) higher than S = 2 (1.00) (Figures 18-19). Figures 20-21 portray that the streamlines for stretching velocity ratio (α = 0.5, and 1.0). It is observed that the streamline difference for is 1.02 whilst α = 1.0 is 1.09. Thus, the amount energy flow in α = 0.5 > α = 1.0. Figures 22-23 show the streamlines for Bi (Bi = 0.3, and 0.6). There observed an equal amount of energy flow in both the cases.
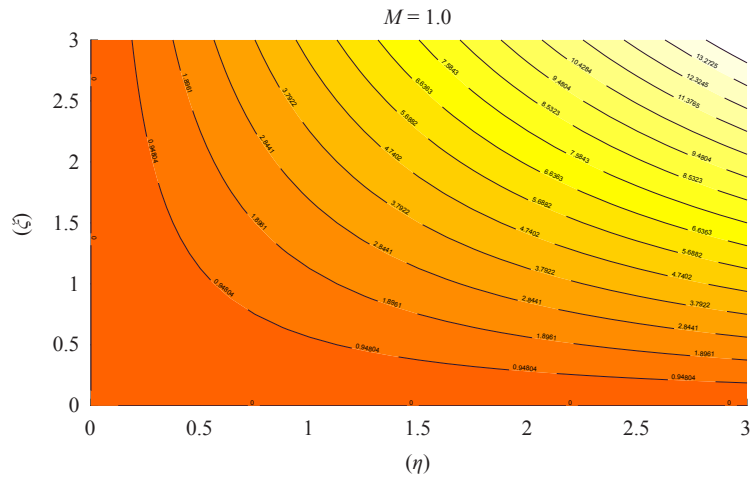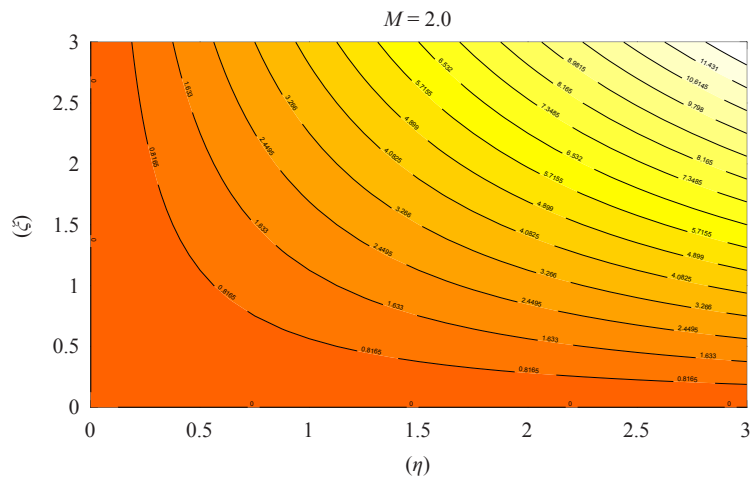
Figure 16. Streamline for ternary fluid flow $M = 1.0$
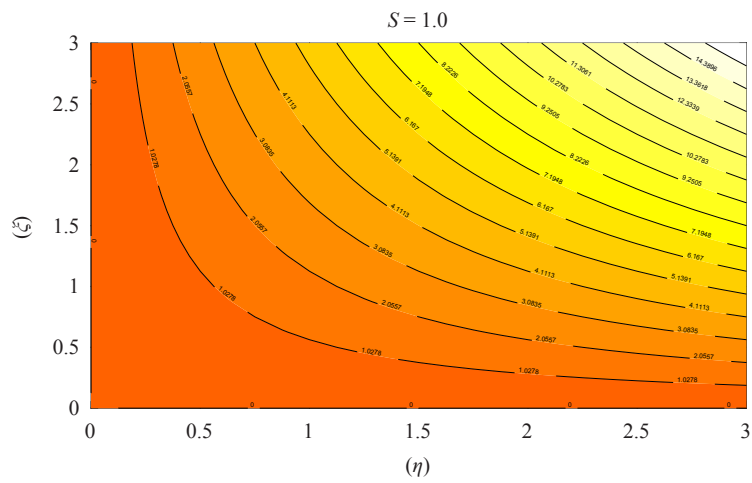

Figure 17. Streamline for ternary fluid flow $M = 2.0$
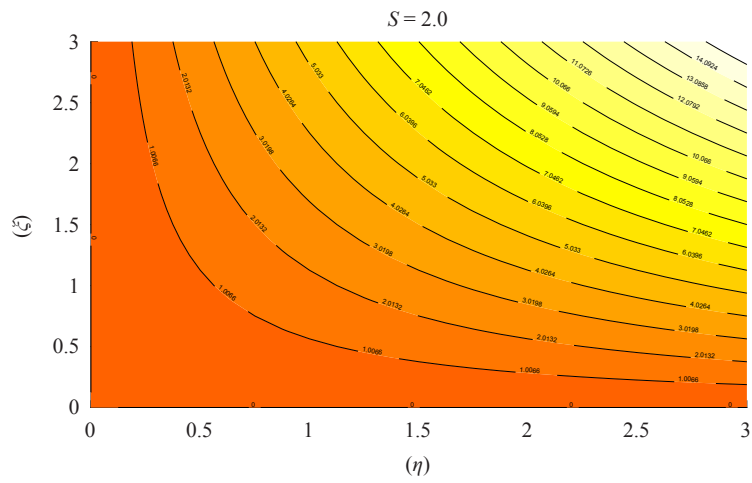

Figure 18. Streamline for ternary fluid flow $S = 1.0$
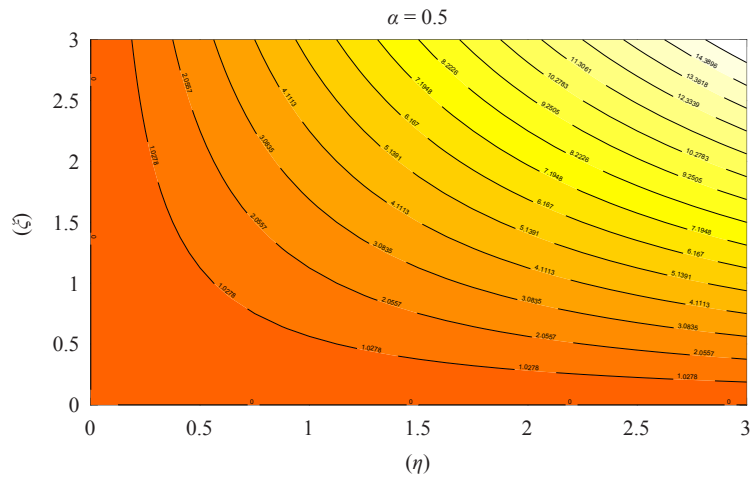
Figure 19. Streamline for ternary fluid flow $S = 2.0$

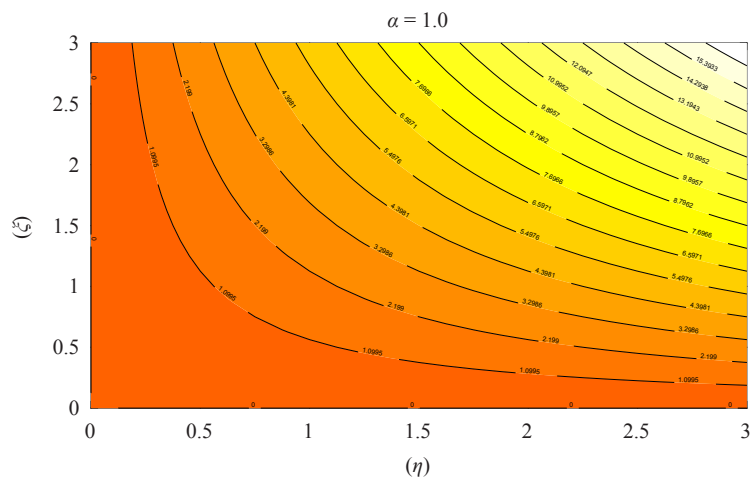**Figure 20.** Streamline for ternary fluid flow $\alpha = 0.5$

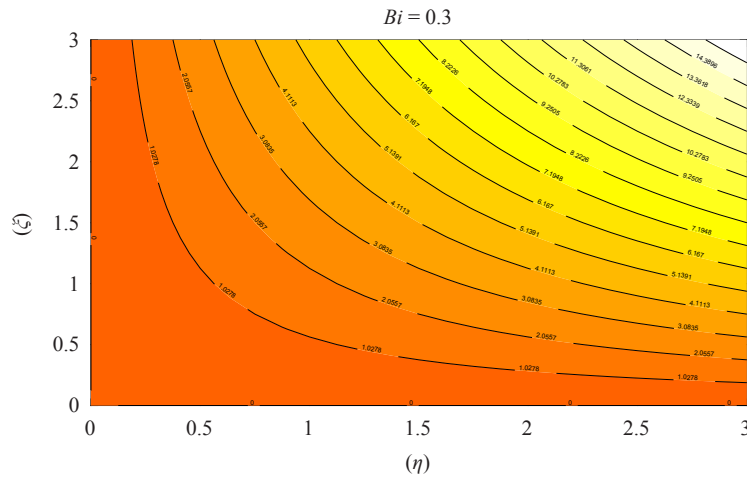**Figure 21.** Streamline for ternary fluid flow $\alpha = 1.0$

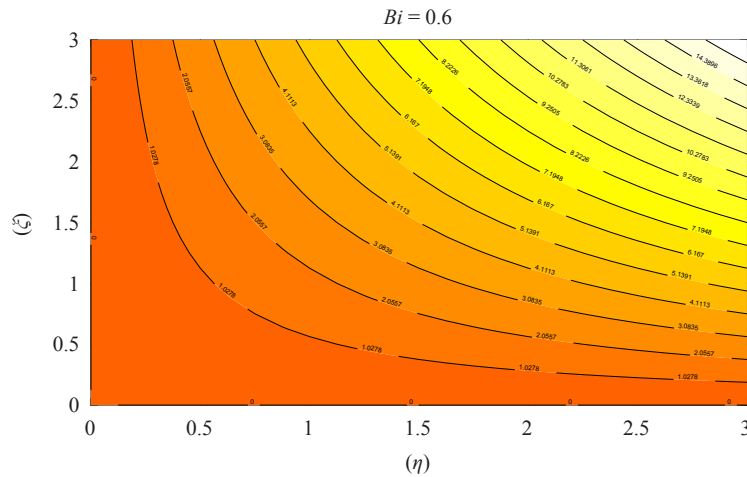**Figure 22.** Streamline for ternary fluid flow $Bi = 0.3$

Figure 23. Streamline for ternary fluid flow $Bi = 0.6$

6. Conclusion

The present study examines radiative unsteady irrotational, incompressible ternary hybrid nanofluid flow with convective heat transfer across a axisymmetric stretched sheet, as well as MHD and an unstable non-uniform heat source and sink. An ODE system is obtained from the flow obeying PDEs with self-similarity variables. Using the MATLAB programme, an implicit Keller Box numerical strategy is implemented and the results are produced. A comparison of HNF ($Fe_3O_4 + Ag/H_2O$) and THNF ($Fe_3O_4 + Ag + Al_2O_3/H_2O$) nanoparticles suspended in water is studied and their behaviour for varied affecting flow field parameters are numerically computed and explained through graphs and tables. Some important results are listed here. The viscous flow case heat transfer rate is higher and same in iron and aluminium oxides whereas for silver, the value is less

(1) Magnetic nanoparticles help in targeted delivery of drugs particularly to the brain. Application of external magnetic field makes the drugs which are encapsulated within nanoparticles can be directly suspended to the brain and controlled release can be done. This reduces the need for frequent dosing and improves drug efficacy.

(2) The ternary hybrid nanoflow ($Fe_3O_4 + Ag + Al_2O_3/H_2O$) transmits more energy for increasing volume fractions, comparing to the hybrid nanofluid ($Fe_3O_4 + Ag/H_2O$).

(3) The study reveals the fact that metal oxides transfer more heat from the system than that of metals.

(4) The estimated error of heat transfer rate is higher in alumina nanoflow followed by silver and iron oxide nanofluid flows.

(5) The streamlines are equally spaced, but the energy flow amount is higher for the case M, $S = 1$ than M, $S = 2$. But in the case of stretching ratio parameter, the amount energy flow in $\alpha = 0.5 > \alpha = 1.0$. An equal amount of energy flow is observed for $Bi = 0.3, 0.6$.

(6) Axial wall drag coefficient seems higher than transverse direction.

(7) Stretching ratio velocity accelerates along axial direction whereas the transversal friction decelerates. Variable magnetic force decreases the skin friction coefficient values.

(8) Unsteadiness ratio also increments the wall shear stresses.

(9) Energy generation improvisation also increments the coefficient of axial and transverse drag friction.

(10) Nano-particles volume fractions improves, the energy transmission rate of iron oxide nanoflow increases for the range $0.01 \leq \phi_1\phi_2\phi_3 \leq 0.06$.

(11) For viscous flow case heat transfer rate is higher and same in iron and aluminium oxides whereas for silver, the value is less.

Data availability statement

Data sharing not applicable to this article as no datasets were generated or analysed during the current study.

Authors contribution

Dr Poornima T and Vinothkumar B contributed equally to the design, implementation and analysis of the research and to the writing of the manuscript.

Statements on ethical standards

This article does not contain any studies involving human participants and animals performed by any of the authors.

Conflict of interest

The authors declare no competing financial interest.

References

[1] Sakiadis BC. Boundary-layer behavior on continuous solid surfaces: I. Boundary-layer equations for two-dimensional and axisymmetric flow. *AIChE Journal*. 1961; 7(1): 26-28. Available from: https://doi.org/10.1002/aic.690070108.

[2] Li S, Puneeth V, Saeed AM, Singhal A, Al-Yarimi FA, Khan MI, et al. Analysis of the Thomson and Troian velocity slip for the flow of ternary nanofluid past a stretching sheet. *Scientific Reports*. 2023; 13(1): 2340. Available from: https://doi.org/10.1038/s41598-023-29485-0.

[3] Souayeh B, Ramesh K. Numerical scrutinization of ternary nanofluid flow over an exponentially stretching sheet with gyrotactic microorganisms. *Mathematics*. 2023; 11(4): 981. Available from: https://doi.org/10.3390/math11040981.

[4] Devi SSU, Devi SA. Numerical investigation of three-dimensional hybrid Cu-Al$_2$O$_3$/water nanofluid flow over a

stretching sheet with effecting Lorentz force subject to Newtonian heating. *Canadian Journal of Physics*. 2016; 94(5): 490-496. Available from: https://doi.org/10.1139/cjp-2015-0799.

[5]   Prasad KV, Vaidya H, Vajravelu K, Rashidi MM. Effects of variable fluid properties on MHD flow and heat transfer over a stretching sheet with variable thickness. *Journal of Mechanics*. 2017; 33(4): 501-512. Available from: https://doi.org/10.1017/jmech.2016.101.

[6]   Choi SU, Eastman JA. *Enhancing thermal conductivity of fluids with nanoparticles*. United States: N. p.; 1995. p.84938. Available from: https://www.osti.gov/servlets/purl/196525.

[7]   Khan WA, Pop I. Boundary-layer flow of a nanofluid past a stretching sheet. *International Journal of Heat and Mass Transfer*. 2010; 53(11-12): 2477-2483. Available from: https://doi.org/10.1016/j.ijheatmasstransfer.2010.01.032.

[8]   Alrihieli H. Thermal and concentration slip impact on the dissipative Casson-Maxwell nanofluid flow due to a stretching sheet with heat generation and thermal radiation. *The European Physical Journal Plus*. 2023; 138(10): 916. Available from: https://doi.org/10.1140/epjp/s13360-023-04525-w.

[9]   Kumar M, Kumar NN, Mondal PK. Irreversibility analysis of hydromagnetic viscoelastic Ag-Al$_2$O$_3$/water hybrid nanofluid over a stretching sheet. *Proceedings of the Institution of Mechanical Engineers, Part E: Journal of Process Mechanical Engineering*. 2023; 86(1). Available from: https://doi.org/10.1177/09544089231193586.

[10] Rao S, Deka P. A numerical study on heat transfer for MHD flow of radiative Casson nanofluid over a porous stretching sheet. *Latin American Applied Research-an International Journal*. 2023; 53(2): 129-136. Available from: https://doi.org/10.52292/j.laar.2023.950.

[11] Elatter S, Khan U, Zaib A, Ishak A, Saleh W, Abed AM. Scrutinization of waste discharge concentrations in eyring-powell nanofluid past a deformable horizontal plane surface. *Water*. 2023; 15(19): 3419. Available from: https://doi.org/10.3390/w15193419.

[12] Gopinathan SM, Kumar PV, Ibrahim SM, Lorenzini G. Impact on casson nanofluid flow across an inclined, slanted surface by radiation, energy and mass transfer. *Journal of Advanced Research in Fluid Mechanics and Thermal Sciences*. 2023; 108(1): 184-202. Available from: https://doi.org/10.37934/arfmts.108.1.184202.

[13] Sharanayya, Biradar S. Magnetized dissipative casson nanofluid flow over a stretching sheet with heat source/sink and soret effect under porous medium. *BioNanoScience*. 2023; 13(4): 2103-2121. Available from: https://doi.org/10.1007/s12668-023-01184-0.

[14] Khashi'ie NS, Roşca NC, Roşca AV, Pop I. Dual solutions on MHD radiative three-dimensional bidirectional nanofluid flow over a non-linearly permeable shrinking sheet. *Alexandria Engineering Journal*. 2023; 71(6): 401-411. Available from: https://doi.org/10.1016/j.aej.2023.03.066.

[15] Hayat U, Shaiq S, Shahzad A. *A Comparative Study of Thin Film Flow of Fe$_3$O$_4$ And Al$_2$O$_3$ Nanoparticles over Stretching Surface Under the Effect of Viscous Dissipation and Magnetohydrodynamics (MHD)*. Research Square; 2023. Available from: https://doi.org/10.21203/rs.3.rs-2693183/v1.

[16] Kumar MNK, Mondal PK. Irreversibility analysis of hydromagnetic viscoelastic Ag-Al$_2$O$_3$/water hybrid nanofluid over a stretching sheet. *Proceedings of the Institution of Mechanical Engineers, Part E: Journal of Process Mechanical Engineering*. 2023; 86. Available from: https://doi.org/10.1177/09544089231193586.

[17] Isa SSPM, Parvin S, Arifin NM, Ali FM, Ahmad K. Soret-dufour effects on the water-based hybrid nanofluid flow with nanoparticles of alumina and copper. *Malaysian Journal of Mathematical Sciences*. 2023; 17(3): 1823-8343. Available from: https://doi.org/10.47836/mjms.17.3.04.

[18] Reddy PS, Sreedevi P, Chamkha AJ. Hybrid nanofluid heat and mass transfer characteristics over a stretching/shrinking sheet with slip effects. *Journal of Nanofluids*. 2023; 12(1): 251-260. Available from: https://doi.org/10.1166/jon.2023.1996.

[19] Alabdulhadi S, Abu Bakar S, Ishak A, Waini I, Ahmed SE. Effect of buoyancy force on an unsteady thin film flow of Al$_2$O$_3$/water nanofluid over an inclined stretching sheet. *Mathematics*. 2023; 11(3): 739. Available from: https://doi.org/10.3390/math11030739.

[20] Javadzadeh S, Almasi H, Alizadeh-Khaledabad M, Azizi S. Immobilization of Al$_2$O$_3$ and Fe$_3$O$_4$ nanoparticles on cellulose and chitosan nanopapers for selective adsorption of free fatty acids from edible oil. *Polymer Bulletin*. 2024; 81: 2043-2067. Available from: https://doi.org/10.1007/s00289-023-04798-2.

[21] Sreenivasulu P, Poornima T, Reddy NB, Reddy MG. A numerical analysis on UCM dissipated nanofluid imbedded carbon nanotubes influenced by inclined Lorentzian force along with non-uniform heat source/sink. *Journal of Nanofluids*. 2019; 8(5): 1076-1084. Available from: https://doi.org/10.1166/jon.2019.1665.

[22] Sreenivasulu P, Bhaskar RN, Poornima T. Variable thermal conductivity influence on hydromagnetic flow past a stretching cylinder in a thermally stratified medium with heat source/sink. *Frontiers in Heat and Mass Transfer* (FHMT). 2017; 9(1): 20. Available from: https://doi.org/10.5098/hmt.9.20.

[23] Sreenivasulu P, Poornima T, Reddy PBA. Soret and Dufour effects on MHD non-Darcian radiating convective flow of micropolar fluid past an inclined surface with non-uniform surface heat source or sink and chemical reaction. *IOP Conference Series: Materials Science and Engineering*. 2017; 263: 062014. Available from: https://doi.org/10.1088/1757-899X/263/6/062014.

[24] Paul A, Nath JM, Das TK. Thermally stratified Cu-Al$_2$O$_3$/water hybrid nanofluid flow with the impact of an inclined magnetic field, viscous dissipation, and heat source/sink across a vertically stretching cylinder. *ZAMM-Journal of Applied Mathematics and Mechanics*. 2023; 104(2): e202300084. Available from: https://doi.org/10.1002/zamm.202300084.

[25] Asogwa KK, Khan I. Radiating and electromagnetic nanofluids flow over an exponentially accelerated Riga plate with heat sink. *Waves in Random and Complex Media*. Taylor & Francis Group. 2023. p.1-22. Available from: https://doi.org/10.1080/17455030.2023.2265493.

[26] Alqawasmi K, Alharbi KAM, Farooq U, Noreen S, Imran M, Akgül A, et al. Numerical approach toward ternary hybrid nanofluid flow with nonlinear heat source-sink and Fourier heat flux model passing through a disk. *International Journal of Thermofluids*. 2023; 18: 100367. Available from: https://doi.org/10.1016/j.ijft.2023.100367.

[27] He K, Ma Y, Yang B, Liang C, Chen X, Cai C. The efficacy assessments of alkylating drugs induced by nano-Fe$_3$O$_4$/CA for curing breast and hepatic cancer. *Spectrochimica Acta Part A: Molecular and Biomolecular Spectroscopy*. 2017; 173: 82-86. Available from: https://doi.org/10.1016/j.saa.2016.08.047.

[28] Ma M, Yan F, Yao M, Wei Z, Zhou D, Yao H, et al. Template-free synthesis of hollow/porous organosilica-Fe$_3$O$_4$ hybrid nanocapsules toward magnetic resonance imaging-guided high-intensity focused ultrasound therapy. *ACS Applied Materials & Interfaces*. 2016; 8(44): 29986-29996. Available from: https://doi.org/10.1021/acsami.6b10370.

[29] Sohail M, Chu YM, El-Zahar ER, Nazir U, Naseem T. Contribution of joule heating and viscous dissipation on three-dimensional flow of Casson model comprising temperature dependent conductance utilizing shooting method. *Physica Scripta*. 2021; 96(8): 085208. Available from: https://doi.org/10.1088/1402-4896/ac00e5.

[30] Ahmad I, Zan-Ul-Abadin Q, Faisal M, Loganathan K, Javed T, Namgyel N. Convective heat transport in bidirectional water driven hybrid nanofluid using blade shaped cadmium telluride and graphite nanoparticles under electro magnetohydrodynamics process. *Journal of Mathematics*. 2022; 2022: 4471450. Available from: https://doi.org/10.1155/2022/4471450.

[31] Muhammad T, Alsaedi A, Hayat T, Shehzad SA. A revised model for Darcy-Forchheimer three-dimensional flow of nanofluid subject to convective boundary condition. *Results in Physics*. 2017; 7: 2791-2797. Available from: https://doi.org/10.1016/j.rinp.2017.07.052.

[32] Manjunatha S, Puneeth V, Gireesha BJ, Chamkha AJ. Theoretical study of convective heat transfer in ternary nanofluid flowing past a stretching sheet. *Journal of Applied and Computational Mechanics*. 2022; 8(4): 1279-1286. Available from: https://doi.org/10.22055/JACM.2021.37698.3067.

[33] Puneeth V, Manjunatha S, Makinde OD, Gireesha BJ. Bioconvection of a radiating hybrid nanofluid past a thin needle in the presence of heterogeneous-homogeneous chemical reaction. *Journal of Heat Transfer*. 2021; 143(4): 042502. Available from: https://doi.org/10.1115/1.4049844.

[34] Liu IC, Andersson HI. Heat transfer over a bidirectional stretching sheet with variable thermal conditions. *International Journal of Heat and Mass Transfer*. 2008; 51(15-16): 4018-4024. Available from: https://doi.org/10.1016/j.ijheatmasstransfer.2007.10.041.

[35] Singh SP, Kumar M, Yaseen M, Rawat SK. Ternary hybrid nanofluid (TiO$_2$-SiO$_2$-MoS$_2$/kerosene oil) flow over a rotating disk with quadratic thermal radiation and Cattaneo-Christov model. *Journal of Central South University*. 2023; 30(4): 1262-1278. Available from: https://doi.org/10.1007/s11771-023-5303-y.

[36] Yaseen M, Rawat SK, Shah NA, Kumar M, Eldin SM. Ternary hybrid nanofluid flow containing gyrotactic microorganisms over three different geometries with Cattaneo-Christov model. *Mathematics*. 2023; 11(5): 1237. Available from: https://doi.org/10.3390/math11051237.

[37] Rawat SK, Yaseen M, Pant M, Ujarari CS, Joshi D, Chaube S, et al. Designing soft computing algorithms to study heat transfer simulation of ternary hybrid nanofluid flow between parallel plates in a parabolic trough solar collector: Case of artificial neural network and particle swarm optimization. *International Communications in Heat and Mass Transfer*. 2023; 148: 107011. Available from: https://doi.org/10.1016/j.icheatmasstransfer.2023.107011.

[38] Ali B, Ali L, Abdal S, Asjad MI. Significance of Brownian motion and thermophoresis influence on dynamics of Reiner-Rivlin fluid over a disk with non-Fourier heat flux theory and gyrotactic microorganisms: A Numerical approach. *Physica Scripta*. 2021; 96(9): 094001. Available from: https://doi.org/10.1088/1402-4896/ac02f0.

[39] Khan SA, Ali B, Eze C, Lau KT, Ali L, Chen J, et al. Magnetic dipole and thermal radiation impact on stagnation

point flow of micropolar based nanofluids over a vertically stretching sheet: Finite element approach. *Processes*. 2021; 9(7): 1089. Available from: Available from: https://doi.org/10.3390/pr9071089.